mathematics

MDPI

Article

Influence of the Schottky Junction on the Propagation Characteristics of Shear Horizontal Waves in a Piezoelectric Semiconductor Semi-Infinite Medium

Xiao Guo [1,*], Yilin Wang [1], Chunyu Xu [2], Zibo Wei [2] and Chenxi Ding [3]

[1] School of Mathematics and Physics, University of Science and Technology Beijing, Beijing 100083, China; m202310731@xs.ustb.edu.cn
[2] Department of Applied Mechanics, University of Science and Technology Beijing, Beijing 100083, China; b20200379@xs.ustb.edu.cn (C.X.); b20190362@xs.ustb.edu.cn (Z.W.)
[3] School of Civil and Resource Engineering, University of Science and Technology Beijing, Beijing 100083, China; dingcx@ustb.edu.cn
* Correspondence: xiaoguo@ustb.edu.cn

Abstract: In this paper, a theoretical model of the propagation of a shear horizontal wave in a piezoelectric semiconductor semi-infinite medium is established using the optimized spectral method. First, the basic equations of the piezoelectric semiconductor semi-infinite medium are derived with the consideration of biased electric fields. Then, considering the propagation of a shear horizontal wave in the piezoelectric semiconductor semi-infinite medium, two equivalent mathematical models are established. In the first mathematical model, the Schottky junction is theoretically treated as an electrically imperfect interface, and an interface characteristic length is utilized to describe the interface effect of the Schottky junction. To legitimately confirm the interface characteristic length, a second mathematical model is established, in which the Schottky junction is theoretically treated as an electrical gradient layer. Finally, the dispersion and attenuation curves of shear horizontal waves are numerically calculated using these two mathematical models to discuss the influence of the Schottky junction on the dispersion and attenuation characteristics of shear horizontal waves. Utilizing the equivalence of these two mathematical models and the above numerical results, the numerical value of the interface characteristic length is reliably legitimately confirmed; this value is independent of the thickness of the upper metal layer, the doping concentration of the lower n-type piezoelectric semiconductor substrate, and biasing electric fields. Only the biasing electric field parallel to the Schottky junction can provide an evident influence on the attenuation characteristics of shear horizontal waves and enhance the interface effect of the Schottky junction. Since the second mathematical model is also a validation of our previous mathematical model established through the state transfer equation method, some numerical results calculated using these two mathematical models are compared with those obtained using the previous method to verify the correctness and superiority of the research work presented in this paper. Since these two mathematical models can better calculate the dispersion and attenuation curves of high-frequency waves in micro- and nano-scale piezoelectric semiconductor materials, the establishment of mathematical models and the revelation of physical mechanisms are fundamental to the analysis and optimization of micro-scale resonators, energy harvesters, and amplifications.

Keywords: piezoelectric semiconductor; Schottky junction; interface effect; shear horizontal wave; spectral method

MSC: 74H15

check for updates

Citation: Guo, X.; Wang, Y.; Xu, C.; Wei, Z.; Ding, C. Influence of the Schottky Junction on the Propagation Characteristics of Shear Horizontal Waves in a Piezoelectric Semiconductor Semi-Infinite Medium. *Mathematics* **2024**, *12*, 560. https://doi.org/10.3390/math12040560

Academic Editors: Hongjie Li and Xianchao Wang

Received: 26 December 2023
Revised: 22 January 2024
Accepted: 5 February 2024
Published: 13 February 2024

Copyright: © 2024 by the authors. Licensee MDPI, Basel, Switzerland. This article is an open access article distributed under the terms and conditions of the Creative Commons Attribution (CC BY) license (https://creativecommons.org/licenses/by/4.0/).

1. Introduction

Surface acoustic waves (SAWs) are elastic waves that propagate on a solid surface, including Rayleigh waves propagating on the surface of a substrate and decaying along

the depth direction of a semi-infinite medium [1,2], Love waves propagating in a layer over a substrate [3–5], and so on. As SAWs have been widely used in nondestructive testing, biological experiments, sensors, and seismology, studying the propagation of SAWs on the surface of a solid medium or in a layer is of great importance. During the propagation of SAWs in piezoelectric materials, the piezoelectric effect leads to variation in coupled mechanical displacement and electric potential. Resulting from the semiconductor effect, the variation in electric potential can lead to the migration and diffusion of hole and electron carriers in some practical piezoelectric materials, i.e., piezoelectric semiconductors (PSCs). Due to piezoelectric and semiconductor effects, PSCs have been used to make devices for energy harvesting and acoustic wave amplification. Based on the classical piezoelectric basic equations with respect to stress and electric displacement, some additional equations concerning charge carrier current density are theoretically added [6–9], which have been utilized to investigate the propagation of generalized Rayleigh SAWs in a PSC half-space [1] and a PSC thin film over an elastic half-space [10], bulk waves in a PSC slab sandwiched by two piezoelectric half-spaces [11] and a PSC half-space [12], and shear-horizontal (SH) waves in single-layered and multilayered PSC plates [13].

As a result of the different doping methods used, some practical PSCs can be either p-type or n-type PSCs, e.g., zinc oxide (ZnO), while some practical PSCs can only be n-type PSCs, e.g., gallium nitride (GaN). When an n-type PSC and metal are bonded together, a Schottky junction appears inevitably at the interface between these two bonded solids [14,15]. Compared with the physical properties of the bulk material, the Schottky junction often has special physical properties. For instance, the steady electron carrier concentrations inside the Schottky junction can vary dramatically, which may lead to drastic changes in the electric potential and electron carrier concentration due to the piezoelectric effect and the semiconductor effect. The influence of the Schottky junction on the propagation characteristics of SAWs should also be considered with the decrease in the geometric dimensions of the metal and PSC employed. Compared with the above literature, the discussion of the influence of Schottky junctions on the propagation characteristics of a shear horizontal wave is relatively lacking; this motivated our previous research work [16], in which the dispersion and attenuation characteristics of a shear horizontal wave in an n-type PSC substrate with a metal layer were studied. The Schottky junction that appeared at the interface between the PSC substrate and the metal layer was considered an electrical gradient layer.

On the other hand, in order to describe the propagation characteristics of SAWs in micro or nanometer-scale materials, the surface and interface effect theory has been established, in which the surface or interface can be regarded as an imperfect interface that leads to a jump in the wave motion quantities between the two sides of the surface or interface [17,18]. With the consideration of the piezoelectric effect, surface or interface imperfect boundary conditions, governing equations, and interface characteristic lengths were introduced, and then some surface and interface piezoelectric theories were also established and utilized to investigate the propagation characteristics of elastic waves in micro- or nanometer-scale piezoelectric materials [19]. Based on Hamilton's principle and a variational approach, Wang et al. established a generalized dynamic model to depict the wave propagation properties in SAW nano-devices [19]. Utilizing surface elasticity, surface piezoelectricity, and surface permittivity, the surface effect was considered to investigate the Love wave propagation in a typical surface acoustic wave device composed of a piezoelectric ceramic transducer film and an aluminum substrate and the shear horizontal vibration of a piezoelectric plate. Based on the surface/interface elasticity (effect), Zhu et al. derived formulations and carried out the calculation of the wave motion characteristics of SH and Lamb waves in layered nanostructures [20]. It was found that the surface/interface effect can be significant when the wavenumber is large and the thickness of the layer is small, as these characteristics affect the dispersion curves, mode shapes, and kinetic and strain energy on the wave. Making use of the dual variable and position method, Tian et al. investigated the propagation characteristics of SH waves in multilayered PSC plates

with imperfect interfaces and discussed the effect of stacking sequences and imperfect interfaces [13]. It was observed that the mechanical imperfect interface can increase the real part of the wavenumber and decrease the imaginary part of the wavenumber for the 1st and 2nd modes, while the electric or electric current imperfect interface has nearly no influence on the dispersion and attenuation curves. Under the mathematical framework of surface/interface elasticity theory, Enzevaee and Shodja formulated the propagation of the torsional surface waves in a medium consisting of a functionally graded substrate bonded to a thin piezoelectric over-layer [21]. It is observed that the surface/interface effects result in a reduction in the phase velocity and the phase velocity reduces by increasing surface/interface parameters for all modes at a specific wave number. Based on the transfer matrix method and the Bloch theorem, Guo et al. studied the influence of the interface effect on the dispersion relation of anti-plane elastic waves in nano-scale one dimensional piezoelectric and PSC phononic crystal [22]. It is found that homo- and hetero-junctions can be approximately treated as rigid imperfect interfaces, which can enhance the width of band-gaps of anti-plane elastic waves, especially for high-frequency short-wavelength anti-plane elastic waves. Based on surface effect of nanostructures and first-order shear deformation theory, Zhang et al. developed a PSC nanoplate model to investigate the influence of surface effect on the natural characteristics and electromechanical responses of the nanoplate subjected to dynamic forces [23]. It is found that surface effect causes the stiffness to be larger, the natural frequencies to be larger, and the piezoelectric effect to be stronger of the nanoplate. Based on the Gurtin-Murdoch surface model, Li et al. conduct an analysis of horizontally polarized shear (SH) waves propagating in an infinite n-type PSC plate with nano-thickness and elaborate the influence of the surface effect, initial electron concentration, and thickness of the PSC plate on the propagation characteristics of SH waves, such as frequency spectrum, phase velocity, and cut-off frequency [24]. It is found that the propagation characteristics of SH waves are size-dependent, and the macroscopic effective shear rigidity is softened at the nanoscale due to surface effect, which thus leads to the reduction of the frequency and phase velocity of SH waves.

Since the geometrical thickness of the Schottky junction is common at the micro-scale which is much smaller than that of the body materials, it can also be treated as an electrically imperfect interface without geometrical thickness but with piezoelectric and semiconductor effects. Based on the physical properties of the Schottky junction and the existing interface piezoelectric theories, the theoretical model of the interface effect of the Schottky junction can also be established to better investigate the influence of the Schottky junction on the propagation characteristics of SAW in micro or nanometer-scale PSC materials, which motivates this paper's work. First, considering the coupling mechanical displacement, electric potential, and charge carrier perturbation, it is mathematically derived that the basic equations of a PSC semi-infinite medium in Section 2, which consists of a lower n-type PSC substrate, an upper grounded metal layer, and a Schottky junction that appears at the interface between these two regions. Two biasing electric fields are further considered in the basic equations of the lower n-type PSC substrate, which provides evident influence on the physical properties of the Schottky junction. Then, through the spectral method [25–27], two equivalent mathematical models are established to investigate the dispersion and attenuation characteristics of the shear horizontal wave that propagates in this PSC semi-infinite medium, instead of the state transfer equation method. Searching for complex roots of complex transcendental equations can be avoided, and the numerical calculation of the dispersion and attenuation curves of the shear horizontal wave is transformed into solving the eigenvalues. To improve the efficiency of the above numerical calculation, the calculating intervals of definite integrals are adjusted reasonably. In the first mathematical model established in Section 3, the Schottky junction is considered as a two-dimensional electrically imperfect interface without geometrical thickness but with piezoelectric and semiconductor characteristics. To legitimately confirm the interface characteristic length that describes the electrically imperfect interface boundary conditions of the Schottky junction, the second mathematical model is established in Section 4, in which the Schottky

junction is considered as an electrical gradient layer. Therefore, the second mathematical model is also a validation of our previous mathematical model. Finally, based on the above two equivalent mathematical models, the numerical results of the dispersion and attenuation curves of shear horizontal waves are provided in Section 5. The numerical value and variation law of the interface characteristic length are also legitimately confirmed and studied. Some numerical results are compared our previous numerical results to verify the correctness and superiority of the research work in this paper. After that, the conclusion remarks are given in Section 6.

2. Problem Formulation and Basic Equations

Consider a PSC semi-infinite medium, formed by a lower n-type PSC substrate and an upper grounded metal layer, as shown in Figure 1. The upper grounded metal layer is isotropic. The lower n-type PSC substrate is transversely isotropic in the Oxy plane. The z-direction is the polarization direction. The thickness of the upper grounded metal layer H is at the micro-scale. Both the upper metal layer and lower PSC substrate are homogeneous. Therefore, a Schottky junction appears at the interface between these two regions, in which the steady electron carrier concentration is inhomogeneous along the y axis. The geometrical thickness of the Schottky junction is y_n, which is much smaller than that of the upper metal layer. The horizontal and vertical biasing electric fields applied to the PSC semi-infinite medium are $\overline{E}_x$ and $\overline{E}_y$, respectively. Consider the propagation of the shear horizontal wave in this PSC substrate in the Oxy plane along the x axis. The Schottky junction and biasing electric fields provide evident influence on the dispersion and attenuation characteristics of the shear horizontal wave. To establish the mathematical models of the shear horizontal wave that propagates in this piezoelectric semiconductor semi-infinite medium and investigate the influence of the Schottky junction on the dispersion and attenuation characteristics of the shear horizontal wave, the basic equations of the upper metal layer and lower PSC substrate are mathematically derived in this section. To distinguish these two regions in the latter formulation, the physical parameters of these two regions are indicated by the superscript 'U' and 'L', respectively.

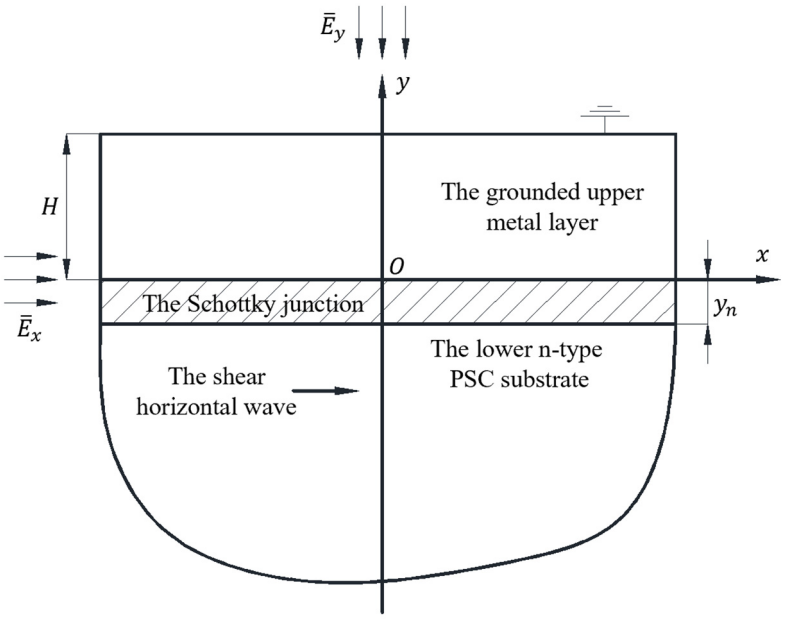


Figure 1. Propagation of the shear horizontal wave in a PSC semi-infinite medium.

Under the supposition of small deformations and the quasi-static electric field approximation and with the consideration of biasing electric fields, the constitutive equations of the lower n-type PSC substrate [11,12] are

$$\sigma_{ij}^{L} = c_{ijkl}^{L} u_{l,k}^{L} + e_{kij}^{L} \phi_{,k}^{L}, D_{k}^{L} = e_{kij}^{L} u_{j,i}^{L} - \varepsilon_{kl}^{L} \phi_{,l}^{L},$$

$$J_{k}^{L} = -q\overline{n}^{L} \mu_{kl}^{L} \phi_{,l}^{L} + qn^{L} \mu_{kl}^{L} \overline{E}_{l} + qd_{kl}^{L} n_{,l}^{L} \tag{1}$$

where u_{l}^{L}, ϕ^{L}, n^{L}, σ_{ij}^{L}, D_{k}^{L}, and J_{k}^{L} are the displacement vector, electric potential scalar, perturbations of electron carrier concentration, Cauchy stress tensor, electric displacement vector and electron carrier current density vector, respectively. With the consideration of the piezoelectric and semiconductor effects, c_{ijkl}^{L}, e_{kij}^{L}, ε_{kl}^{L}, μ_{kl}^{L}, and d_{kl}^{L} are the elastic, piezoelectric, dielectric, electron carrier migration, and electron carrier diffusion parameter tensors, respectively. The carrier charge is $q = 1.602 \times 10^{-19}$C. The steady electron carrier concentration is $\overline{n}^{L}$, which is a function of the space coordinate y and the vertical biasing electric field $\overline{E}_{y}$ mathematically

$$\overline{n}^{L} = \begin{cases} N_{D}^{L} exp\left\{ \frac{\mu_{yy}^{L}}{d_{yy}^{L}} \left[\frac{qN_{D}^{L}}{e_{yyz}^{L2}/c_{yzyz}^{L} + \varepsilon_{yy}^{L}} \left(-\frac{1}{2}y^{2} - y_{n}y - \frac{1}{2}y_{n}^{2} \right) - 2\overline{E}_{y}(y + y_{n}) \right] \right\} & -y_{n} \le y \le 0 \\ N_{D}^{L} & -\infty < y \le -y_{n} \end{cases} \tag{2}$$

where N_{D}^{L} are the donor concentration i.e., the doping concentration, in the lower n-type PSC substrate. The geometrical thickness of the Schottky junction is

$$y_{n} = \sqrt{\frac{2\left(e_{yyz}^{L2}/c_{yzyz}^{L} + \varepsilon_{yy}^{L}\right)(W^{U} - W^{L})}{q^{2}N_{D}^{L}}} \tag{3}$$

where W^{U} and W^{L} are the work functions for the metal and n-type PSC substrate, respectively. The detailed derivation of the above two physical quantities is shown in the Appendix A. Based on plane strain assumption, the displacements, electric potential, and carrier concentration perturbation of the shear horizontal wave are all functions of space coordinates x and y and time coordinate t mathematically

$$u_{x}^{L} = u_{y}^{L} = 0, u_{z}^{L} = u_{z}^{L}(x, y, t), \phi^{L} = \phi^{L}(x, y, t), n^{L} = n^{L}(x, y, t) \tag{4}$$

Inserting Equation (4) into Equation (1) leads to the Cauchy stress components

$$\sigma_{zx}^{L} = \sigma_{xz}^{L} = c_{xzxz}^{L} \frac{\partial u_{z}^{L}}{\partial x} + e_{yyz}^{L} \frac{\partial \phi^{L}}{\partial x}, \sigma_{zy}^{L} = \sigma_{yz}^{L} = c_{yzyz}^{L} \frac{\partial u_{z}^{L}}{\partial y} + e_{yyz}^{L} \frac{\partial \phi^{L}}{\partial y} \tag{5}$$

electric displacement components

$$D_{x}^{L} = e_{xxz}^{L} \frac{\partial u_{z}^{L}}{\partial x} - \varepsilon_{xx}^{L} \frac{\partial \phi^{L}}{\partial x}, D_{y}^{L} = e_{yyz}^{L} \frac{\partial u_{z}^{L}}{\partial y} - \varepsilon_{yy}^{L} \frac{\partial \phi^{L}}{\partial y} \tag{6}$$

and electron carrier current density components

$$J_{x}^{L} = -q\overline{n}^{L} \mu_{xx}^{L} \frac{\partial \phi^{L}}{\partial x} + qn^{L} \mu_{xx}^{L} \overline{E}_{x} + qd_{xx}^{L} \frac{\partial n^{L}}{\partial x},$$

$$J_{y}^{L} = -q\overline{n}^{L} \mu_{yy}^{L} \frac{\partial \phi^{L}}{\partial y} + qn^{L} \mu_{yy}^{L} \overline{E}_{y} + qd_{yy}^{L} \frac{\partial n^{L}}{\partial y} \tag{7}$$

With the consideration of the piezoelectric and semiconductor effects, the governing equations of the lower n-type PSC substrate [11,12] are

$$\sigma_{ij,i}^{L} = \rho^{L}\frac{\partial^2 u_j^L}{\partial t^2}, D_{k,k}^{L} = -qn^{L}, J_{k,k}^{L} = q\frac{\partial n^L}{\partial t} \tag{8}$$

where ρ^L is the mass density. Inserting Equations (5)–(7) into Equation (8) leads to the governing equations expressed by the displacements, electric potential and carrier concentration perturbations

$$\begin{gathered} c_{yzyz}^{L}\left(\frac{\partial^2}{\partial x^2}+\frac{\partial^2}{\partial y^2}\right)u_z^L + e_{yyz}^{L}\left(\frac{\partial^2}{\partial x^2}+\frac{\partial^2}{\partial y^2}\right)\phi^L = \rho\frac{\partial^2 u_z^L}{\partial t^2} \\ e_{yyz}^{L}\left(\frac{\partial^2}{\partial x^2}+\frac{\partial^2}{\partial y^2}\right)u_z^L - \varepsilon_{yy}^{L}\left(\frac{\partial^2}{\partial x^2}+\frac{\partial^2}{\partial y^2}\right)\phi^L = -qn^L \\ -\overline{n}^{L'}\mu_{yy}^{L}\frac{\partial \phi^L}{\partial y} - \overline{n}^{L}\mu_{yy}^{L}\left(\frac{\partial^2}{\partial x^2}+\frac{\partial^2}{\partial y^2}\right)\phi^L + \left(\mu_{yy}^{L}\overline{E}_x\frac{\partial}{\partial x}+\mu_{yy}^{L}\overline{E}_y\frac{\partial}{\partial y}\right)n^L \\ +d_{yy}^{L}\left(\frac{\partial^2}{\partial x^2}+\frac{\partial^2}{\partial y^2}\right)n^L = \frac{\partial n^L}{\partial t} \end{gathered} \tag{9}$$

Without the piezoelectric and semiconductor effects, under the supposition of small deformations, the constitutive equations of the upper metal layer [28] are

$$\sigma_{ij}^{U} = c_{ijkl}^{U}u_{l,k}^{U} \tag{10}$$

where u_j^U, σ_{ij}^U, and c_{ijkl}^U are the displacement vector, Cauchy stress tensor, and elastic parameter tensor of the upper metal layer, respectively. Based on the plane strain assumption, the displacement component u_j^U is also a function of space coordinates x and y and time coordinate t mathematically

$$u_x^U = u_y^U = 0, u_z^U = u_z^U(x,y,t) \tag{11}$$

Inserting Equation (11) into Equation (10) leads to the Cauchy stress components of the upper metal layer

$$\sigma_{zx}^{U} = \sigma_{xz}^{U} = c_{xzxz}^{U}\frac{\partial u_z^U}{\partial x}, \sigma_{zy}^{U} = \sigma_{yz}^{U} = c_{yzyz}^{U}\frac{\partial u_z^U}{\partial y} \tag{12}$$

The governing equation of the upper metal layer [28] is

$$\sigma_{ij,i}^{U} = \rho^{U}\frac{\partial^2 u_j^U}{\partial t^2} \tag{13}$$

where ρ^U is the mass density of the upper metal layer. Inserting Equation (12) into Equation (13) leads to

$$c_{yzyz}^{U}\left(\frac{\partial^2}{\partial x^2}+\frac{\partial^2}{\partial y^2}\right)u_z^U = \rho^{U}\frac{\partial^2 u_z^U}{\partial t^2} \tag{14}$$

On the surface $y = H$, consider the surface condition of the upper metal layer with respect to the Cauchy stress [28]

$$\sigma_{yz}^{U}\Big|_{y=H^-} = 0 \tag{15}$$

Equations (9), (14) and (15) provide the basic equations of the PSC semi-infinite medium, which can be utilized to establish the mathematical model of the shear horizontal wave that propagates in this PSC semi-infinite medium through the spectral method. However, as the core part of the PSC semi-infinite medium, the basic equations of the

Schottky junction are not fully given. Therefore, when the Schottky junction is treated as an electrically imperfect interface or an electrical gradient layer, two different groups of basic equations can be given and two equivalent mathematical models can be established in the next two sections. In order to improve the computational efficiency of these two mathematical models, we reasonably modify some calculating intervals of definite integrals in the spectral method.

3. The First Mathematical Model

According to Equation (4), assume the mathematical expressions of the displacement, electric potential, and carrier concentration perturbation of the shear horizontal wave in the lower n-type PSC substrate as

$$\begin{aligned}&\left\{u_z^L(x,y,t),\phi^L(x,y,t),n^L(x,y,t)\right\}\\&=\left\{U_z^L(y),U_\phi^L(y),U_n^L(y)\right\}exp\left[\beth\left(k^Lx-\omega^Lt\right)\right],-\infty<y\le 0\end{aligned}\tag{16}$$

where k^L and ω^L are the apparent wave number component and angular frequency of the shear horizontal wave in the lower n-type PSC substrate, respectively. Based on the spectral method [25–27], the Laguerre polynomials Q_m are used to expand these three undetermined amplitudes U_z^L, U_ϕ^L, and U_n^L, which are all functions of the space coordinate y mathematically

$$\begin{aligned}U_z^L(y)&=\sum_{m=0}^{\infty}z_m^LR_m^L(y)\approx\sum_{m=0}^{M}z_m^LR_m^L(y),\\U_\phi^L(y)&=\sum_{m=0}^{\infty}\phi_m^LR_m^L(y)\approx\sum_{m=0}^{M}\phi_m^LR_m^L(y),\\U_n^L(y)&=\sum_{m=0}^{\infty}n_m^LR_m^L(y)\approx\sum_{m=0}^{M}n_m^LR_m^L(y),-\infty<y\le 0\end{aligned}\tag{17}$$

where z_m^L, ϕ_m^L and n_m^L are expansion coefficients and

$$R_m^L(y)=e^{\frac{y}{2}}Q_m(-y),R_m^{L\prime}(-\infty)=R_l^L(-\infty)=0,Q_m(\overline{y})=\frac{e^{\overline{y}}}{m!}\frac{d^m}{d\overline{y}^m}\left(\overline{y}^me^{-\overline{y}}\right)\tag{18}$$

Inserting Equations (16) and (17) into Equation (9), multiplying both sides by $R_l^L(y)$ and taking the definite integrals lead to

$$\begin{aligned}&\omega^2\rho^L\sum_{m=0}^{M}z_m^L\int_{-\infty}^{0}R_m^L(y)R_l^L(y)dy\\&+c_{yzyz}^L\sum_{m=0}^{M}z_m^L\left(R_m^{L\prime}(0)R_l^L(0)-R_m^L(0)R_l^{L'}(0)+\int_{-\infty}^{0}R_m^L(y)R_l^{L''}(y)dy\right)\\&+e_{yyz}^L\sum_{m=0}^{M}\phi_m^L\left(R_m^{L\prime}(0)R_l^L(0)-R_m^L(0)R_l^{L'}(0)+\int_{-\infty}^{0}R_m^L(y)R_l^{L''}(y)dy\right)\\&=k^2c_{yzyz}^L\sum_{m=0}^{M}z_m^L\int_{-\infty}^{0}R_m^L(y)R_l^L(y)dy+k^2e_{yyz}^L\sum_{m=0}^{M}\phi_m^L\int_{-\infty}^{0}R_m^L(y)R_l^L(y)dy\end{aligned}\tag{19}$$

$$\begin{aligned}&e_{yyz}^L\sum_{m=0}^{M}z_m^L\left(R_m^{L\prime}(0)R_l^L(0)-R_m^L(0)R_l^{L'}(0)+\int_{-\infty}^{0}R_m^L(y)R_l^{L''}(y)dy\right)\\&-\varepsilon_{yy}^L\sum_{m=0}^{M}\phi_m^L\left(R_m^{L'}(0)R_l^L(0)-R_m^L(0)R_l^{L'}(0)+\int_{-\infty}^{0}R_m^L(y)R_l^{L''}(y)dy\right)\\&+q\sum_{m=0}^{M}n_m^L\int_{-\infty}^{0}R_m^L(y)R_l^L(y)dy=k^2e_{yyz}^L\sum_{m=0}^{M}z_m^L\int_{-\infty}^{0}R_m^L(y)R_l^L(y)dy\\&-k^2\varepsilon_{yy}^L\sum_{m=0}^{M}\phi_m^L\int_{-\infty}^{0}R_m^L(y)R_l^L(y)dy\end{aligned}\tag{20}$$

$$
\begin{aligned}
&i\omega \sum_{m=0}^{M} n_m^L \int_{-\infty}^{0} R_m^L(y) R_l^L(y) dy \\
&-N_D^L \mu_{yy}^L \sum_{m=0}^{M} \phi_m^L \left(R_m^{L'}(0) R_l^L(0) - R_m^L(0) R_l^{L'}(0) + \int_{-\infty}^{0} R_m^L(y) R_l^{L''}(y) dy \right) \\
&+d_{yy}^L \sum_{m=0}^{M} n_m^L \left(R_m^{L'}(0) R_l^L(0) - R_m^L(0) R_l^{L'}(0) + \int_{-\infty}^{0} R_m^L(y) R_l^{L''}(y) dy \right) \\
&+ik\overline{E}_x \mu_{yy}^L \sum_{m=0}^{M} n_m^L \int_{-\infty}^{0} R_m^L(y) R_l^L(y) dy \\
&+\overline{E}_y \mu_{yy}^L \sum_{m=0}^{M} n_m^L \left(R_m^L(0) R_l^L(0) - \int_{-\infty}^{0} R_m^L(y) R_l^{L'}(y) dy \right) \\
&= -N_D^L \mu_{yy}^L k^2 \sum_{m=0}^{M} \phi_m^L \int_{-\infty}^{0} R_m^L(y) R_l^L(y) dy \\
&+d_{yy}^L k^2 \sum_{m=0}^{M} n_m^L \int_{-\infty}^{0} R_m^L(y) R_l^L(y) dy
\end{aligned} \tag{21}
$$

According to Equation (11), assume the mathematical expressions of the displacement of the shear horizontal wave in the upper metal layer as

$$u_z^U(x, y, t) = U_z^U(y) exp\left[i\left(k^U x - \omega^U t \right) \right], 0 \le y \le H \tag{22}$$

where k^U and ω^U are the apparent wave number component and angular frequency of the shear horizontal wave in the upper metal layer, respectively. Based on the spectral method [25–27], the Legendre polynomials P_m are used to expand the undetermined amplitude U_z^U, which is also a function of the space coordinate y mathematically

$$U_z^U(y) = \sum_{m=0}^{\infty} z_m^U R_m^U(y) \approx \sum_{m=0}^{M} z_m^U R_m^U(y), 0 \le y \le H \tag{23}$$

where z_m^U is expansion coefficients, $m = 0, 1, 2, \cdots, M$. M is an integer.

$$R_m^U(y) = P_m\left(\frac{2y - H}{H} \right), P_m(\overline{y}) = \frac{d^m}{2^m m! d\overline{y}^m} \left(\overline{y}^2 - 1 \right)^m \tag{24}$$

Inserting Equations (22) and (23) into Equation (14), multiplying both sides by $R_l^U(y)$ and taking the definite integrals leads to

$$
\begin{aligned}
&\rho^U \omega^2 \sum_{m=0}^{M} z_m^U \int_0^H R_m^U(y) R_l^U(y) dy \\
&+c_{yzyz}^U \sum_{m=0}^{M} z_m^U \left(R_m^{U\prime}(y) R_l^U(y) \Big|_0^H - R_m^U(y) R_l^{U'}(y) \Big|_0^H + \int_0^H R_m^U(y) R_l^{U''}(y) dy \right) \\
&= c_{yzyz}^U k^2 \sum_{m=0}^{M} z_m^U \int_0^H R_m^U(y) R_l^U(y) dy
\end{aligned} \tag{25}
$$

Considering the geometrical thickness of the Schottky junction is much smaller than that of the upper metal layer, i.e., $y_n \ll H$, the Schottky junction is treated as a two-dimensional electrically imperfect interface without geometrical thickness but with piezoelectric and semiconductor effects in this mathematical model. The interface boundary condition to the Cauchy stress and electric displacement at the Schottky junction is

$$\left\{ n_i \sigma_{ij}^L, n_i D_i^L \right\} \Big|_{y=0^-} - \left\{ n_i \sigma_{ij}^U, 0 \right\} \Big|_{y=0^+} = \left\{ 0, D_{l,l}^I \right\} \tag{26}$$

where D_l^I is the electric displacement vector of the electrically imperfect interface,

$$D_l^I = e_{lij}^I u_{j,i}^I - \varepsilon_{lj}^I \phi_{,j}^I \tag{27}$$

and e_{lij}^I and ε_{lj}^I are the interface piezoelectric and dielectric parameter tensors, respectively. The interface boundary condition to the displacement and electric potential at the boundary $y = 0$ is

$$\left\{u_z^L, \phi^L\right\}\Big|_{y=0^-} = \left\{u_z^U, 0\right\}\Big|_{y=0^+} = \left\{u_z^I, \phi^I\right\} \tag{28}$$

where u_z^I and ϕ^I are the displacement vector and electric potential of the electrically imperfect interface, respectively. Inserting the interface normal vector $n_i = \{0, 1, 0\}$ into Equation (26) leads to

$$\left\{\sigma_{yz}^L, D_y^L\right\}\Big|_{y=0^-} - \left\{\sigma_{yz}^U, 0\right\}\Big|_{y=0^+} = \left\{0, D_{x,x}^I\right\} \tag{29}$$

Inserting Equation (28) into Equation (27) leads to

$$D_x^I = e_{yyz}^I u_{z,x}^I \tag{30}$$

and

$$e_{yyz}^I = f_e^L e_{yyz}^L \tag{31}$$

where f_e^L is the interface characteristic length related to the interface piezoelectric parameter. Inserting Equations (30) and (31) into Equations (28) and (29) leads to

$$\left\{u_z^L, \phi^L, \sigma_{yz}^L\right\}\Big|_{y=0^-} = \left\{u_z^U, 0, \sigma_{yz}^U\right\}\Big|_{y=0^+} \tag{32}$$

$$\left(e_{yyz}^L \frac{\partial u_z^L}{\partial y} - \varepsilon_{yy}^L \frac{\partial \phi^L}{\partial y}\right)\Big|_{y=0^-} = f_e^L e_{yyz}^L \frac{\partial^2 u_z^L}{\partial x^2}\Big|_{y=0^-} \tag{33}$$

Inserting Equations (16), (17), (22), and (23) into Equations (15), (32) and (33) leads to

$$\sum_{m=0}^{M} z_m^U R_m^{U\prime}(H) = 0 \tag{34}$$

$$\sum_{m=0}^{M} z_m^U R_m^U(0) = \sum_{m=0}^{M} z_m^L R_m^L(0) \tag{35}$$

$$\sum_{m=0}^{M} \phi_m^L R_m^L(0) = 0 \tag{36}$$

$$c_{yzyz}^L \sum_{m=0}^{M} z_m^L R_m^{L\prime}(0) + e_{yyz}^L \sum_{m=0}^{M} \phi_m^L R_m^{L\prime}(0) = c_{yzyz}^U \sum_{m=0}^{M} z_m^U R_m^{U\prime}(0) \tag{37}$$

$$e_{yyz}^L \sum_{m=0}^{M} z_m^L R_m^{L\prime}(0) - \varepsilon_{yy}^L \sum_{m=0}^{M} \phi_m^L R_m^{L\prime}(0) = -k^2 f_e^L e_{yyz}^L \sum_{m=0}^{M} z_m^L R_m^L(0) \tag{38}$$

and

$$k^U = k^L = k,\ \omega^U = \omega^L = \omega \tag{39}$$

Inserting Equations (34) and (35) into Equation (25) leads to

$$\rho^U \omega^2 \sum_{m=0}^{M} z_m^U \int_0^H R_m^U(y) R_l^U(y) dy$$

$$-c_{yzyz}^U \sum_{m=0}^{M} z_m^U \left(R_m^{U\prime}(0) R_l^U(0) + R_m^U(H) R_l^{U\prime}(H) - \int_0^H R_m^U(y) R_l^{U\prime\prime}(y) dy\right)$$

$$+c_{yzyz}^{U}\sum_{m=0}^{M} z_m^L R_m^L(0) R_l^{U\prime}(0) = k^2 c_{yzyz}^{U}\sum_{m=0}^{M} z_m^L \int_0^H R_m^U(y) R_l^U(y) dy \tag{40}$$

Inserting Equations (36)–(38) into Equations (19)–(21) leads to

$$\begin{aligned}
&\omega^2\rho^L\sum_{m=0}^{M} z_m^L \int_{-\infty}^{0} R_m^L(y) R_l^L(y) dy \\
&-c_{yzyz}^{L}\sum_{m=0}^{M} z_m^L \left(R_m^L(0) R_l^{L\prime}(0) - \int_{-\infty}^{0} R_m^L(y) R_l^{L''}(y) dy \right) \\
&+e_{yyz}^{L}\sum_{m=0}^{M} \phi_m^L \int_{-\infty}^{0} R_m^L(y) R_l^{L\prime\prime}(y) dy + c_{yzyz}^{U}\sum_{m=0}^{M} z_m^U R_m^{U\prime}(0) R_l^L(0) \\
&= k^2 c_{yzyz}^{L}\sum_{m=0}^{M} z_m^L \int_{-\infty}^{0} R_m^L(y) R_l^L(y) dy + k^2 e_{yyz}^{L}\sum_{m=0}^{M} \phi_m^L \int_{-\infty}^{0} R_m^L(y) R_l^L(y) dy
\end{aligned} \tag{41}$$

$$\begin{aligned}
&e_{yyz}^{L}\sum_{m=0}^{M} z_m^L \left(\int_{-\infty}^{0} R_m^L(y) R_l^{L''}(y) dy - R_m^L(0) R_l^{L\prime}(0) \right) \\
&-\varepsilon_{yy}^{L}\sum_{m=0}^{M} \phi_m^L \int_{-\infty}^{0} R_m^L(y) R_l^{L''}(y) dy + q\sum_{m=0}^{M} n_m^L \int_{-\infty}^{0} R_m^L(y) R_l^L(y) dy \\
&= k^2 e_{yyz}^{L}\sum_{m=0}^{M} z_m^L \int_{-\infty}^{0} R_m^L(y) R_l^L(y) dy - k^2 \varepsilon_{yy}^{L}\sum_{m=0}^{M} \phi_m^L \int_{-\infty}^{0} R_m^L(y) R_l^L(y) dy \\
&+k^2 f_e^L e_{yyz}^{L}\sum_{m=0}^{M} z_m^L R_m^L(0) R_l^L(0)
\end{aligned} \tag{42}$$

$$\begin{aligned}
&i\omega\sum_{m=0}^{M} n_m^L \int_{-\infty}^{0} R_m^L(y) R_l^L(y) dy \\
&-N_D^L \mu_{yy}^{L}\sum_{m=0}^{M} \phi_m^L \left(R_m^{L\prime}(0) R_l^L(0) - R_m^L(0) R_l^{L\prime}(0) + \int_{-\infty}^{0} R_m^L(y) R_l^{L''}(y) dy \right) \\
&+d_{yy}^{L}\sum_{m=0}^{M} n_m^L \left(R_m^{L\prime}(0) R_l^L(0) - R_m^L(0) R_l^{L\prime}(0) + \int_{-\infty}^{0} R_m^L(y) R_l^{L''}(y) dy \right) \\
&+\overline{E}_y \mu_{yy}^{L}\sum_{m=0}^{M} n_m^L \left(R_m^L(0) R_l^L(0) - \int_{-\infty}^{0} R_m^L(y) R_l^{L\prime}(y) dy \right) \\
&+ik\overline{E}_x \mu_{yy}^{L}\sum_{m=0}^{M} n_m^L \int_{-\infty}^{0} R_m^L(y) R_l^L(y) dy \\
&= -N_D^L \mu_{yy}^{L} k^2 \sum_{m=0}^{M} \phi_m^L \int_{-\infty}^{0} R_m^L(y) R_l^L(y) dy \\
&+d_{yy}^{L} k^2 \sum_{m=0}^{M} n_m^L \int_{-\infty}^{0} R_m^L(y) R_l^L(y) dy
\end{aligned} \tag{43}$$

Combining Equations (40)–(43) and letting l changes from 0 to M leads to

$$\omega^2 \boldsymbol{AP} + i\omega \boldsymbol{BP} + \boldsymbol{CP} + ik\boldsymbol{FP} = k^2 \boldsymbol{DP} \tag{44}$$

where the unknown expansion coefficients vector is

$$\boldsymbol{P} = \left\{ z_0^U, z_1^U, \cdots, z_M^U, z_0^L, z_1^L, \cdots, z_M^L, \phi_0^L, \phi_1^L, \cdots, \phi_M^L, n_0^L, n_1^L, \cdots, n_M^L \right\}^T \tag{45}$$

The explicit expressions of coefficient matrices $\boldsymbol{A}$, $\boldsymbol{B}$, $\boldsymbol{C}$, $\boldsymbol{D}$, and $\boldsymbol{F}$ in Equation (44) are given in Appendix A. In order to obtain the dispersion and attenuation characteristics of the shear horizontal wave, define another vector as

$$\boldsymbol{Q} = k\boldsymbol{P} \tag{46}$$

Inserting Equation (46) into Equation (44) leads to

$$\omega^2 \boldsymbol{AP} + i\omega \boldsymbol{BP} + \boldsymbol{CP} = -ik\boldsymbol{FP} + k\boldsymbol{DQ} \tag{47}$$

Combining Equations (46) and (47) leads to

$$\begin{bmatrix} \boldsymbol{O} & \boldsymbol{E} \\ \omega^2\boldsymbol{A}+i\omega\boldsymbol{B}+\boldsymbol{C} & \boldsymbol{O} \end{bmatrix}\begin{bmatrix} \boldsymbol{P} \\ \boldsymbol{Q} \end{bmatrix} = k\begin{bmatrix} \boldsymbol{E} & \boldsymbol{O} \\ -i\boldsymbol{F} & \boldsymbol{D} \end{bmatrix}\begin{bmatrix} \boldsymbol{P} \\ \boldsymbol{Q} \end{bmatrix} \tag{48}$$

where $\boldsymbol{O}$ and $\boldsymbol{E}$ are the null and unit matrices, respectively. Equation (48) is a generalized eigenvalue problem for the apparent wave number component k. Given the numerical values of the angular frequency of the shear horizontal wave ω, the dispersion and attenuation curves of the shear horizontal wave can be obtained. Searching for complex roots of complex transcendental equations in our previous mathematical model established through the state transfer equation method can be avoided mathematically. Since many elements of matrices $\boldsymbol{A}$, $\boldsymbol{B}$, $\boldsymbol{C}$, $\boldsymbol{D}$, and $\boldsymbol{F}$ are related to the definite integrals of Legendre and Laguerre polynomials, the analytical results of the definite integrals of the above two polynomials are given in the Appendix A of this paper. Using these analytic results, the generalized eigenvalue problem in Equation (48) can be calculated efficiently. However, to obtain the dispersion and attenuation curves of the shear horizontal wave, the interface characteristic length f_e^L should be legitimately confirmed. To legitimately confirm the interface characteristic length f_e^L, another equivalent mathematical model is established in Section 4, i.e., the second mathematical model.

4. The Second Mathematical Model

In this mathematical model, the Schottky junction is theoretically treated as an electrical gradient layer, in which the steady electron carrier concentration is a function of the space coordinate y and the vertical biasing electric field $\overline{E}_y$ mathematically, as shown in Equation (2). Therefore, Equation (21) are modified as

$$\begin{aligned} &i\omega\textstyle\sum_{m=0}^{M} n_m^L\int_{-\infty}^{-y_n} R_m^L(y)R_l^L(y)dy - \mu_{yy}^L N_D^L\sum_{m=0}^{M}\phi_m^L\int_{-\infty}^{-y_n} R_m^{L''}(y)R_l^L(y)dy \\ &+d_{yy}^L\textstyle\sum_{m=0}^{M} n_m^L\left(R_m^{L\prime}(0)R_l^L(0) - R_m^L(0)R_l^{L\prime}(0) + \int_{-\infty}^{-y_n} R_m^L(y)R_l^{L''}(y)dy\right) \\ &-d_{yy}^L\textstyle\sum_{m=0}^{M} n_m^L\int_{-y_n}^{0} R_m^{L''}(y)R_l^L(y)dy \\ &+\mu_{yy}^L\textstyle\sum_{m=0}^{M} n_m^L\int_{-\infty}^{-y_n}\left(ik\overline{E}_x R_m^L(y) + \overline{E}_y R_m^{L\prime}(y)\right)R_l^L(y)dy \\ &= -k^2\mu_{yy}^L N_D^L\textstyle\sum_{m=0}^{M}\phi_m^L\int_{-\infty}^{-y_n} R_m^L(y)R_l^L(y)dy \\ &+k^2 d_{yy}^L\textstyle\sum_{m=0}^{M} n_m^L\int_{-\infty}^{-y_n} R_m^L(y)R_l^L(y)dy \end{aligned} \tag{49}$$

It is observed that the integral range of Equation (49) is different from that of Equation (21), i.e., the optimized spectral method. The mathematical reason why we set the integral range of Equation (49) this result is that the steady electron carrier concentration $\overline{n}^L$ is constant in this integral range according to Equation (2), and such mathematical operation can simplify subsequent numerical calculations of definite integrals and improve the computational efficiency of the spectral method. At the boundary $y = 0$, consider the following interface condition [10]

$$\left\{u_z^U, 0, 0, \sigma_{yz}^U\right\}\Big|_{y=0^+} = \left\{u_z^L, \phi^L, n^L, \sigma_{yz}^L\right\}\Big|_{y=0^-} \tag{50}$$

Inserting Equations (16), (17), (22) and (23) into Equations (52) leads to

$$\textstyle\sum_{m=0}^{M} z_m^L R_m^L(0) = \sum_{m=0}^{M} z_m^U R_m^U(0) \tag{51}$$

$$\sum_{m=0}^{M} \phi_m^L R_m^L(0) = 0 \tag{52}$$

$$\sum_{m=0}^{M} n_m^L R_m^L(0) = 0 \tag{53}$$

$$c_{yzyz}^L \sum_{m=0}^{M} z_m^L R_m^{L\prime}(0) + e_{yyz}^L \sum_{m=0}^{M} \phi_m^L R_m^{L\prime}(0) = c_{yzyz}^U \sum_{m=0}^{M} z_m^U R_m^{U\prime}(0) \tag{54}$$

Inserting Equations (52)–(54) into Equations (19), (20) and (49) leads to

$$\begin{aligned} &\omega^2 \rho^L \sum_{m=0}^{M} z_m^L \int_{-\infty}^{0} R_m^L(y) R_l^L(y) dy \\ &-c_{yzyz}^L \sum_{m=0}^{M} z_m^L \left(R_m^L(0) R_l^{L\prime}(0) - \int_{-\infty}^{0} R_m^L(y) R_l^{L''}(y) dy \right) \\ &+e_{yyz}^L \sum_{m=0}^{M} \phi_m^L \int_{-\infty}^{0} R_m^L(y) R_l^{L''}(y) dy + c_{yzyz}^U \sum_{m=0}^{M} z_m^U R_m^{U\prime}(0) R_l^L(0) \\ &= k^2 c_{yzyz}^L \sum_{m=0}^{M} z_m^L \int_{-\infty}^{0} R_m^L(y) R_l^L(y) dy + k^2 e_{yyz}^L \sum_{m=0}^{M} \phi_m^L \int_{-\infty}^{0} R_m^L(y) R_l^L(y) dy \end{aligned} \tag{55}$$

$$\begin{aligned} &e_{yyz}^L \sum_{m=0}^{M} z_m^L \left(R_m^{L\prime}(0) R_l^L(0) - R_m^L(0) R_l^{L\prime}(0) + \int_{-\infty}^{0} R_m^L(y) R_l^{L''}(y) dy \right) \\ &-\varepsilon_{yy}^L \sum_{m=0}^{M} \phi_m^L \left(R_m^{L\prime}(0) R_l^L(0) + \int_{-\infty}^{0} R_m^L(y) R_l^{L''}(y) dy \right) \\ &+q \sum_{m=0}^{M} n_m^L \int_{-\infty}^{0} R_m^L(y) R_l^L(y) dy = k^2 e_{yyz}^L \sum_{m=0}^{M} z_m^L \int_{-\infty}^{0} R_m^L(y) R_l^L(y) dy \\ &-k^2 \varepsilon_{yy}^L \sum_{m=0}^{M} \phi_m^L \int_{-\infty}^{0} R_m^L(y) R_l^L(y) dy \end{aligned} \tag{56}$$

$$\begin{aligned} &i\omega \sum_{m=0}^{M} n_m^L \int_{-\infty}^{-y_n} R_m^L(y) R_l^L(y) dy - \mu_{yy}^L N_D^L \sum_{m=0}^{M} \phi_m^L \int_{-\infty}^{-y_n} R_m^{L''}(y) R_l^L(y) dy \\ &+d_{yy}^L \sum_{m=0}^{M} n_m^L \left(R_m^{L\prime}(0) R_l^L(0) + \int_{-\infty}^{0} R_m^L(y) R_l^{L''}(y) dy \right) \\ &-d_{yy}^L \sum_{m=0}^{M} n_m^L \int_{-y_n}^{0} R_m^{L''}(y) R_l^L(y) dy \\ &+\mu_{yy}^L \sum_{m=0}^{M} n_m^L \int_{-\infty}^{-y_n} \left(ik\overline{E}_x R_m^L(y) + \overline{E}_y R_m^{L\prime}(y) \right) R_l^L(y) dy \\ &= -k^2 \mu_{yy}^L N_D^L \sum_{m=0}^{M} \phi_m^L \int_{-\infty}^{-y_n} R_m^L(y) R_l^L(y) dy \\ &+k^2 d_{yy}^L \sum_{m=0}^{M} n_m^L \int_{-\infty}^{-y_n} R_m^L(y) R_l^L(y) dy \end{aligned} \tag{57}$$

Combining Equations (40) and (55)–(57) and letting l changes from 0 to M leads to

$$\omega^2 \overline{\boldsymbol{A}} \boldsymbol{P} + i\omega \overline{\boldsymbol{B}} \boldsymbol{P} + \overline{\boldsymbol{C}} \boldsymbol{P} + ik\overline{\boldsymbol{F}} \boldsymbol{P} = k^2 \overline{\boldsymbol{D}} \boldsymbol{P} \; a = 1, \tag{58}$$

where the unknown expansion coefficients vector is

$$\boldsymbol{P} = \left\{ z_0^U, z_1^U, \cdots, z_M^U, z_0^L, z_1^L, \cdots, z_M^L, \phi_0^L, \phi_1^L, \cdots, \phi_M^L, n_0^L, n_1^L, \cdots, n_M^L \right\}^T \tag{59}$$

The explicit expressions of coefficient matrices $\overline{\boldsymbol{A}}$, $\overline{\boldsymbol{B}}$, $\overline{\boldsymbol{C}}$, $\overline{\boldsymbol{D}}$, and $\overline{\boldsymbol{F}}$ in Equation (59) are given in Appendix A. In order to obtain the dispersion and attenuation characteristics of the shear horizontal wave, define another one vector as

$$\boldsymbol{Q} = k\boldsymbol{P} \tag{60}$$

Inserting Equation (60) into Equation (58) leads to

$$\omega^2\overline{\boldsymbol{A}}\boldsymbol{P} + i\omega\overline{\boldsymbol{B}}\boldsymbol{P} + \overline{\boldsymbol{C}}\boldsymbol{P} = -ik\overline{\boldsymbol{F}}\boldsymbol{P} + k\overline{\boldsymbol{D}}\boldsymbol{Q} \tag{61}$$

Combining Equations (60) and (61) leads to

$$\begin{bmatrix} \boldsymbol{O} & \boldsymbol{E} \\ \omega^2\overline{\boldsymbol{A}} + i\omega\overline{\boldsymbol{B}} + \overline{\boldsymbol{C}} & \boldsymbol{O} \end{bmatrix} \begin{bmatrix} \boldsymbol{P} \\ \boldsymbol{Q} \end{bmatrix} = k \begin{bmatrix} \boldsymbol{E} & \boldsymbol{O} \\ -i\overline{\boldsymbol{F}} & \overline{\boldsymbol{D}} \end{bmatrix} \begin{bmatrix} \boldsymbol{P} \\ \boldsymbol{Q} \end{bmatrix} \tag{62}$$

Equation (62) is also a generalized eigenvalue problem for the apparent wave number component k without the interface characteristic length f_e^L. Considering these two mathematical models established in Sections 3 and 4 are equivalent, the interface characteristic length f_e^L can be inversely confirmed through the comparison of dispersion and attenuation curves numerically calculated using these two mathematical models in the next section.

5. Numerical Results and Discussion

In this section, the dispersion and attenuation curves of shear horizontal waves are numerically calculated using the mathematical models established in Sections 3 and 4. Meanwhile, the interface characteristic length f_e^L are legitimately confirmed through the comparison of dispersion and attenuation curves calculated using these two equivalent mathematical models. The upper metal layer and lower n-type PSC substrate are defined as Au and ZnO, respectively. The constitutive parameters of these two materials in the Cartesian coordinate system are contained in Table 1 [10]. To study the variation law of the interface characteristic length f_e^L, the thickness of the upper Au layer is taken as 1 μm, 5 μm or 10 μm, respectively, and the doping concentration of the lower n-type ZnO substrate is 1×10^{21} m^{-3}, 5×10^{21} m^{-3}, or 10×10^{21} m^{-3}, respectively. Since the numerical calculation of the dispersion and attenuation curves of shear horizontal waves is transformed into solving the eigenvalues, many eigenvalues that do not belong to the dispersion and attenuation curves of shear horizontal waves are also obtained. To solve the above computational complexity of the spectral method, we set the above numerical calculation examples to compare with our previous research work and to quickly refine the eigenvalues that belong to the dispersion and attenuation curves of shear horizontal waves from the original calculation dates. The horizontal axes of the dispersion and attenuation curves are the dimensionless angular frequency $\overline{\omega} = \omega H/\sqrt{c_{yzyz}^L/\rho^L}$. The vertical axis of the dispersion curve is the wave speed of shear horizontal waves $c = real(\omega/k)$. The vertical axis of the attenuation curve is the dimensionless attenuation parameter $\overline{k} = imag(kH)$.

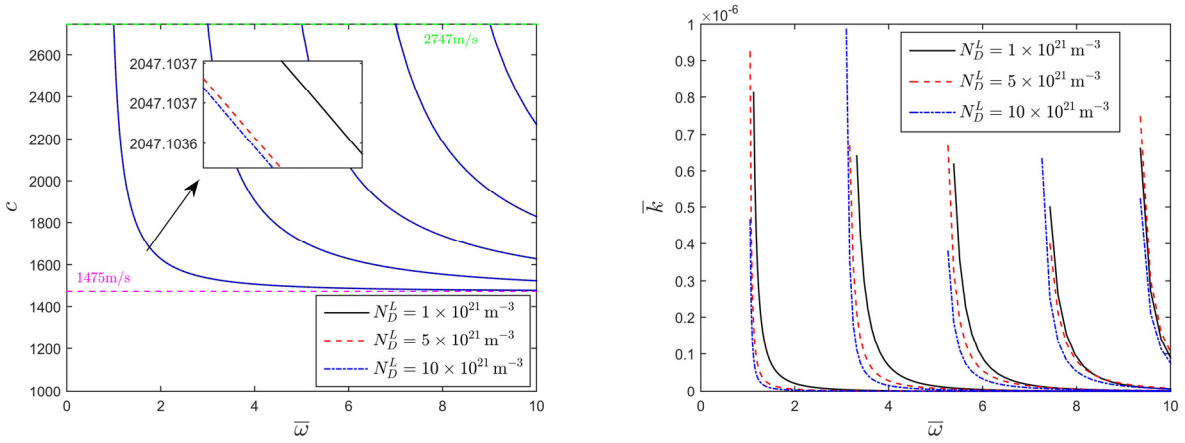
Table 1. The physical constants of Au and n-type ZnO [10].

	c_{yzyz}	ρ	e_{yyz}	ε_{yy}	μ_{yy}	d_{yy}	W
ZnO	43	5700	−0.48	7.61	0.01	2.6	4.45
Au	42	19,300	0	0	0	0	5.1

Note: c_{yzyz}: GPa, ρ: kgm^{-3}, e_{yyz}: cm^{-2}, ε_{yy}: 10^{-11} CV^{-1}m^{-1}, μ_{yy}: m^{2}V^{-1}s^{-1}, d_{yy}: 10^{-4}m^{2}s^{-1}, W: eV.

To verify the correctness and superiority of the research work in this paper, Figure 2 shows the dispersion and attenuation curves of shear horizontal waves calculated by the second mathematical model without the consideration of biasing electric fields, when the thickness of the upper Au layer is 1 μm and the doping concentration of lower n-type ZnO substrate is 1×10^{21} m^{-3}, 5×10^{21} m^{-3}, or 10×10^{21} m^{-3}, respectively. Similar to Figures 2 and 3 in Reference [16], it is also observed from Figure 2a,b that the phase velocities and dimensionless attenuation parameters of the first and second orders shear horizontal wave tend to 1475 m/s and 0 m/s, respectively, with the increase of the dimensionless angular frequency; the phase velocities and dimensionless attenuation parameters of the first and second orders shear horizontal wave both gradually increase with the

increase of the dimensionless angular frequency. At different doping concentrations, the dispersion curves of shear horizontal waves coincide approximately, which means that the Schottky junction has negligible influence on the dispersion characteristic of shear horizontal waves; but the attenuation curves of shear horizontal waves change obviously, which means that the Schottky junction has evident influence on the attenuation characteristic of shear horizontal wave. Therefore, the Schottky junction can be theoretically treated as a two-dimensional electrically imperfect interface. However, different from Figure 2 shown in Reference [16], the phase velocities and dimensionless attenuation parameters of the first order shear horizontal waves don't tend to 2747 m/s and 0 m/s, respectively, when $\overline{\omega} \to 0$. The reason for these numerical calculation results is that the second mathematical model is established using the optimized spectral method. On the one hand, searching for complex roots of complex transcendental equations is transformed into eigenvalue calculation problems; the initial values which are closely related to the complex roots and need to be given in advance are no longer given. On the other hand, the numerical calculation of the transfer matrix of Schottky junction through the truncated Magnus series in Reference [16] is also avoided as the integral interval of Equation (49) is $-\infty < y \leq -y_n$. All the above mathematical operations can reduce the numerical calculation errors and improve the computational efficiency. The robustness of the second mathematical model is better than that of the mathematical model in Reference [16]. So, we can calculate and plot the wider dimensionless angular frequency intervals and higher orders of the dispersion and attenuation curves of shear horizontal waves in this paper.



(**a**) (**b**)

Figure 2. The dispersion and attenuation curves of shear horizontal waves calculated by the second mathematical model without the consideration of biasing electric fields. (**a**) The dispersion curves $H = 1$ μm; (**b**) The attenuation curves $H = 1$ μm.

Since the Schottky junction has evident influence on the attenuation characteristic of shear horizontal wave, the comparisons of the attenuation curves of shear horizontal waves are utilized to legitimately confirm the numerical value of the interface piezoelectric parameter. Figure 3 shows the comparisons of the attenuation curves of shear horizontal waves calculated by the first and second mathematical models without the consideration of biasing electric fields, when the thickness of the upper Au layer is 1 μm, 5 μm, or 10 μm, respectively, and the doping concentration of lower n-type ZnO substrate is 1×10^{21} m^{-3} or 10×10^{21} m^{-3}, respectively. The discrete numerical points are calculated using the first mathematical model, in which the interface characteristic length related to the interface piezoelectric parameter is

$$f_e^L = -0.014774258 \text{ m} \tag{63}$$

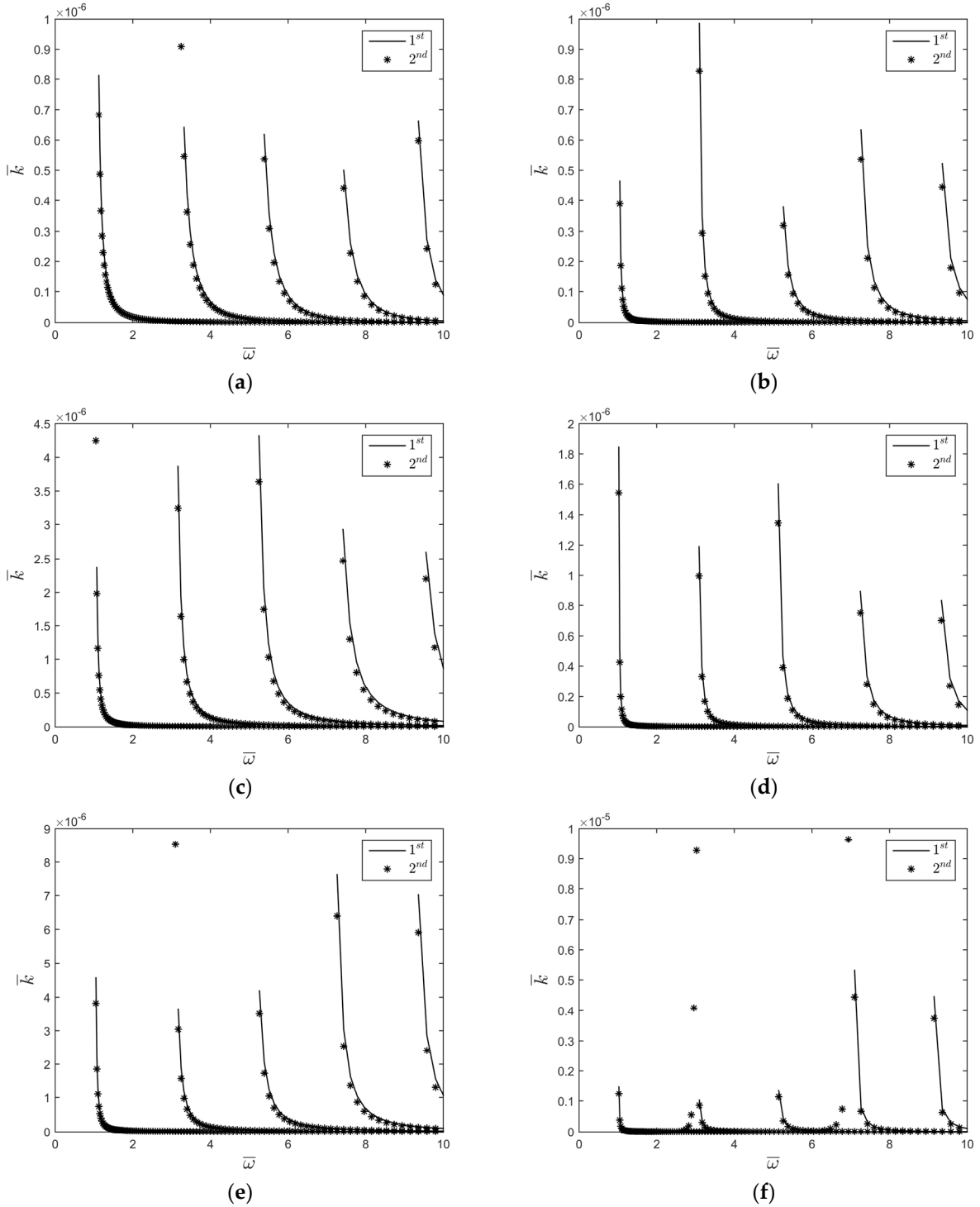


Figure 3. The comparisons of attenuation curves of shear horizontal waves calculated by the first and second mathematical models without the consideration of biasing electric fields. (**a**) The attenuation curves $H = 1$ μm, $N_D^L = 1 \times 10^{21}$ m^{-3}; (**b**) The attenuation curves $H = 1$ μm, $N_D^L = 10 \times 10^{21}$ m^{-3}; (**c**) The attenuation curves $H = 5$ μm, $N_D^L = 1 \times 10^{21}$ m^{-3}; (**d**) The attenuation curves $H = 5$ μm, $N_D^L = 10 \times 10^{21}$ m^{-3}; (**e**) The attenuation curves $H = 10$ μm, $N_D^L = 1 \times 10^{21}$ m^{-3}; (**f**) The attenuation curves $H = 10$ μm, $N_D^L = 10 \times 10^{21}$ m^{-3}.

Because the Schottky junction is theoretically treated as a two-dimensional electrically imperfect interface, there is only one interface characteristic length that needs to be determined. This provides great convenience for the numerical calculations in this section. It is

noted from Equation (63) that the numerical value of f_e^L is negative. This numerical calculation result can be explained by Equations (32) that the sum of the electric displacement of the shear horizontal wave at the boundary $y = 0^-$ and the gradient of the interface electric displacement is exactly equal to 0, which is the electric displacement of the shear horizontal wave at the boundary $y = 0^+$. The continuous curves are also calculated using the second mathematical model. Since these two mathematical models are equivalent, all the discrete numerical points fall on the continuous curves approximately. It is further observed from Figure 3 that the numerical value of f_e^L is independent of the thickness of the upper Au layer and the doping concentration of the lower n-type ZnO substrate. This is because the thickness of the Schottky junction is usually on the order of 10 to the power of -7, which is much smaller than the thickness of the upper Au layer. Due to the upper metal layer being a grounded Au, the electric potential in the whole upper Au layer is zero, which causes the interface electric potential to be zero as well and there is no interface boundary condition related to the semiconductor effect, as shown in Equation (32). Since the interface characteristic length f_e^L is a constant, the first mathematical model is more practical, and can be utilized to investigate the interaction between high-frequency elastic waves and Schottky junctions.

To investigate the influence of biasing electric fields, the following dimensionless biasing electric fields are introduced, namely,

$$\gamma_x = \mu_{yy}^L \overline{E}_x \sqrt{\rho^L / c_{yzyz}^L}, \gamma_y = \mu_{yy}^L \overline{E}_y \sqrt{\rho^L / c_{yzyz}^L} \tag{64}$$

Figures 4 and 5 show the dispersion and attenuation curves of shear horizontal waves with the variation of the above two dimensionless biasing electric fields. It is observed from Figures 4 and 5 that these two biasing electric fields $\overline{E}_x$ and $\overline{E}_y$ have almost no influence on the dispersion characteristic of shear horizontal waves. This numerical calculation result can be explained by Equation (7) that these two biasing electric fields are only related to the carrier's current density components, and the electrical energy accounts for a relatively low proportion of the total energy of shear horizontal waves. While the increase of $\overline{E}_x$ makes the attenuation curves of shear horizontal waves shift towards higher values, which means that the existence of $\overline{E}_x$ can greatly enhance the attenuation characteristics of shear horizontal waves. But the biasing electric field $\overline{E}_y$ has negligible influence on the attenuation characteristic of shear horizontal waves. This is because the direction of the biased electric field $\overline{E}_x$ is the same as the propagation direction of shear horizontal waves, as shown in Figure 1.

Figure 6 shows the comparisons of attenuation curves of shear horizontal waves calculated by the first and second mathematical models with the consideration of biasing electric fields, when the thickness of the upper Au layer is 1 μm, 5 μm, or 10 μm, respectively, and the doping concentration of lower n-type ZnO substrate is $1 \times 10^{21} \mathrm{m}^{-3}$ or 10×10^{21} m^{-3}, respectively. The discrete numerical points and continuous curves are also calculated using the first and second mathematical models, respectively. It is also observed from Figure 6 that all the discrete numerical points fall on the continuous curves approximately, which means that the numerical value of f_e^L in Equation (63) is independent of biasing electric fields. This numerical calculation result can also be explained by Equation (32) that there is no biasing electric field in the electrically imperfect interface boundary condition.

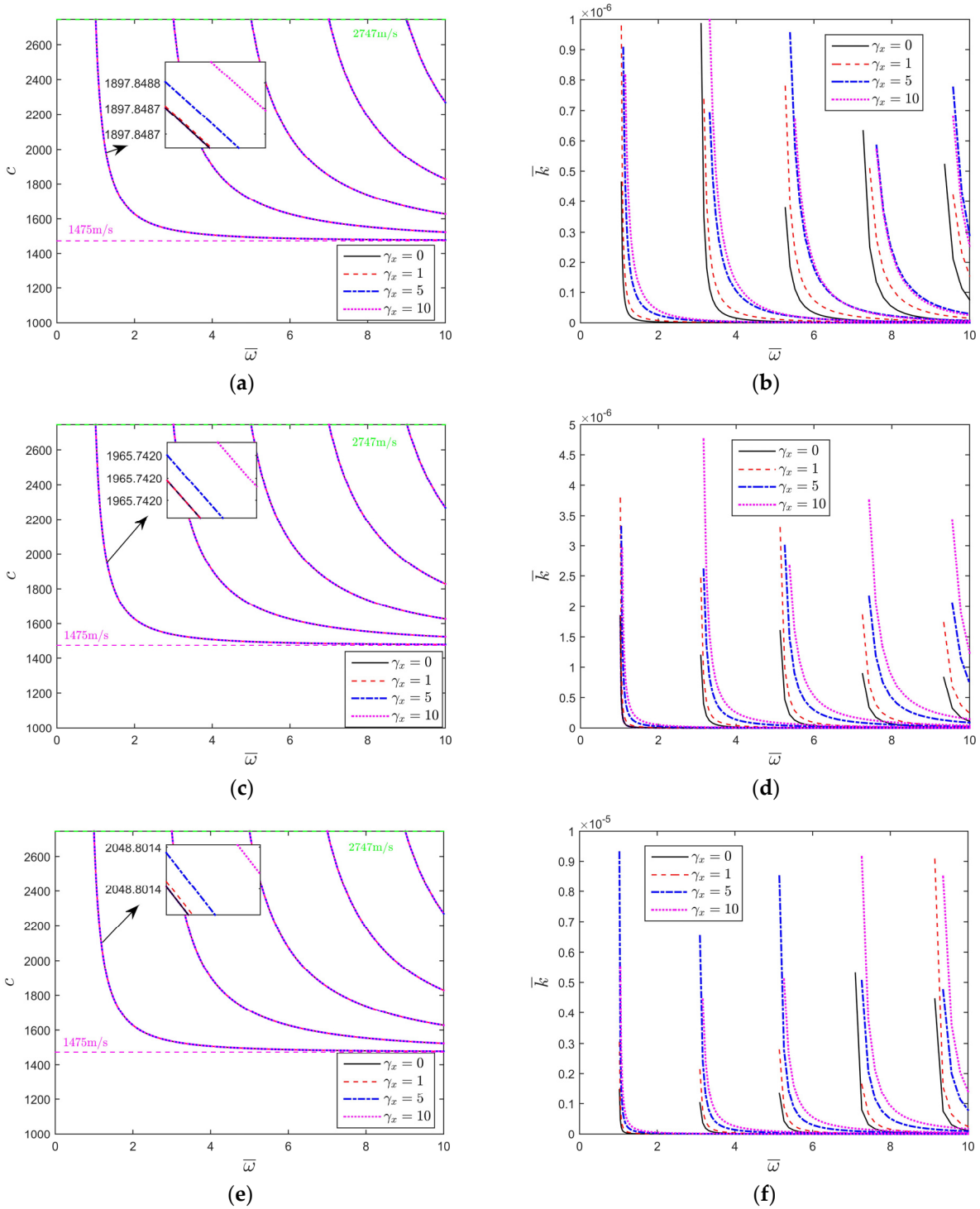


Figure 4. The dispersion and attenuation curves of shear horizontal waves with the variation of the dimensionless biasing electric field γ_x. (**a**) The dispersion curves $H = 1$ μm, $N_D^L = 10 \times 10^{21}$ m^{-3}, $\gamma_y = 0$; (**b**) The attenuation curves $H = 1$ μm, $N_D^L = 10 \times 10^{21}$ m^{-3}, $\gamma_y = 0$; (**c**) The dispersion curves $H = 5$ μm, $N_D^L = 10 \times 10^{21}$ m^{-3}, $\gamma_y = 0$; (**d**) The attenuation curves $H = 5$ μm, $N_D^L = 10 \times 10^{21}$ m^{-3}, $\gamma_y = 0$; (**e**) The dispersion curves $H = 10$ μm, $N_D^L = 10 \times 10^{21}$ m^{-3}, $\gamma_y = 0$; (**f**) The attenuation curves $H = 10$ μm, $N_D^L = 10 \times 10^{21}$ m^{-3}, $\gamma_y = 0$.

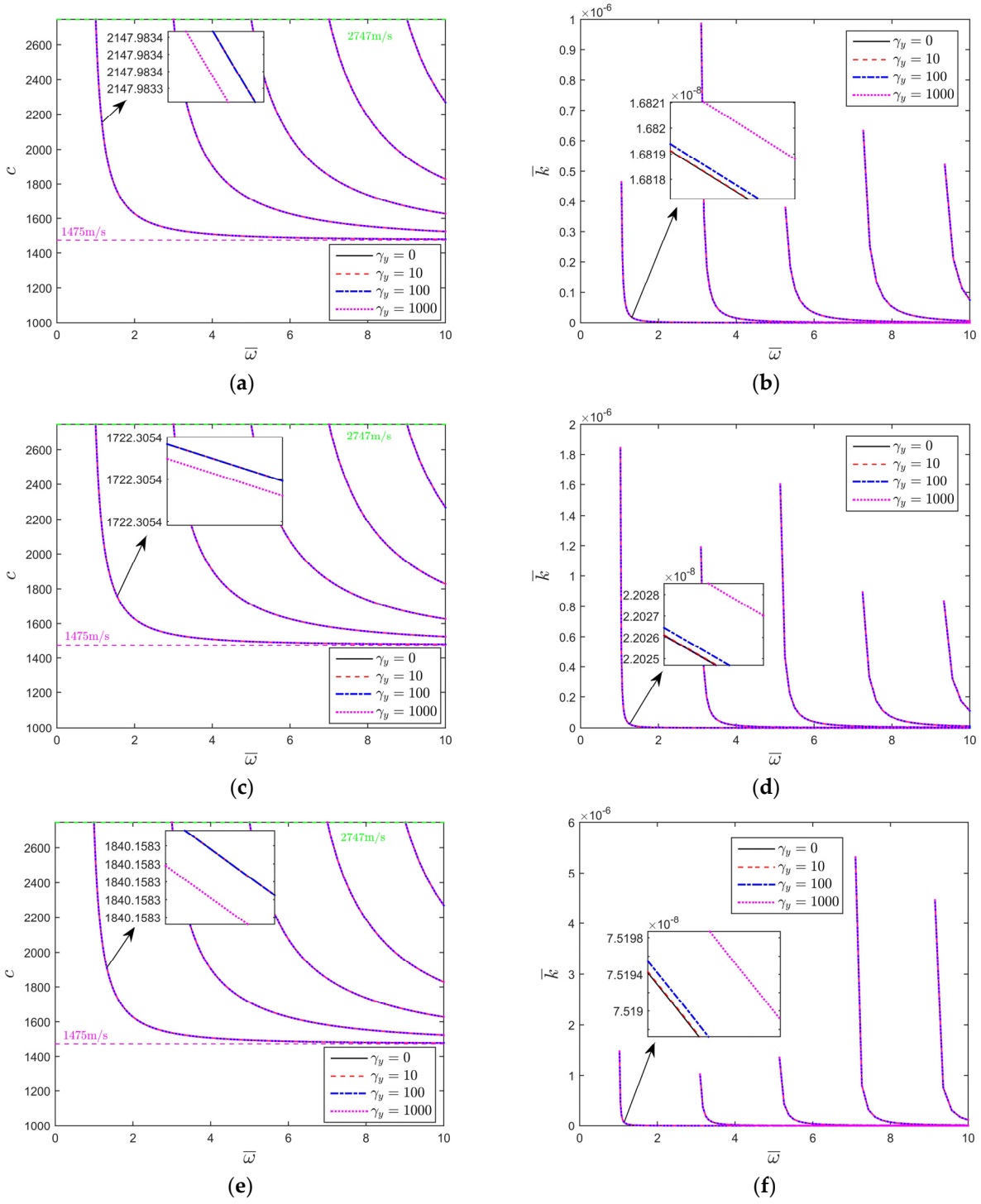


Figure 5. The dispersion and attenuation curves of shear horizontal waves with the variation of the dimensionless biasing electric field γ_y. (**a**) The dispersion curves $H = 1$ μm, $N_D^L = 10 \times 10^{21}$ m^{-3}, $\gamma_x = 0$; (**b**) The attenuation curves $H = 1$ μm, $N_D^L = 10 \times 10^{21}$ m^{-3}, $\gamma_x = 0$; (**c**) The dispersion curves $H = 5$ μm, $N_D^L = 10 \times 10^{21}$ m^{-3}, $\gamma_x = 0$; (**d**) The attenuation curves $H = 5$ μm, $N_D^L = 10 \times 10^{21}$ m^{-3}, $\gamma_x = 0$; (**e**) The dispersion curves $H = 10$ μm, $N_D^L = 10 \times 10^{21}$ m^{-3}, $\gamma_x = 0$; (**f**) The attenuation curves $H = 10$ μm, $N_D^L = 10 \times 10^{21}$ m^{-3}, $\gamma_x = 0$.

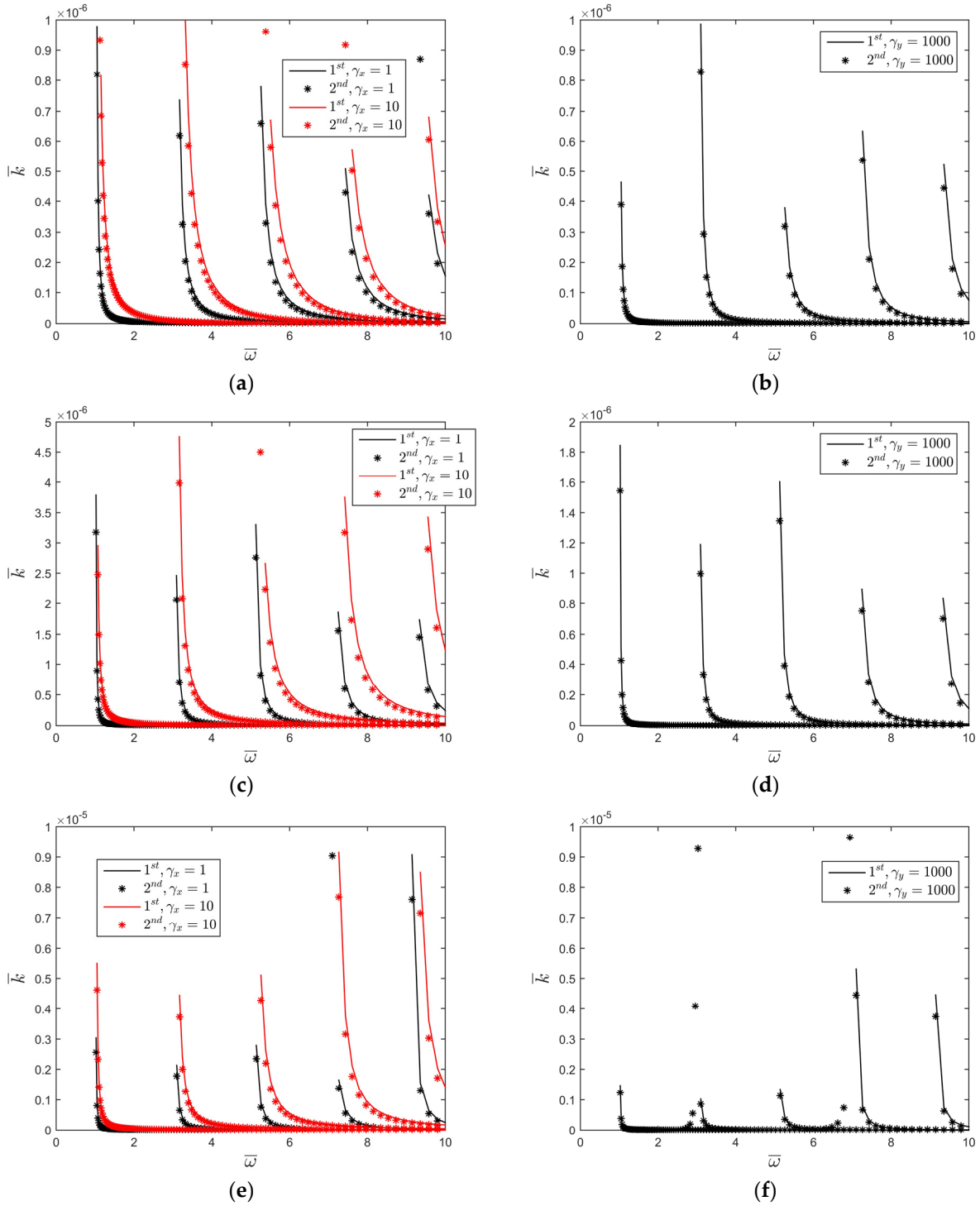


Figure 6. The comparisons of attenuation curves of shear horizontal waves calculated by the first and second mathematical models with the consideration of biasing electric fields. (**a**) The attenuation curves $H = 1$ µm, $N_D^L = 10 \times 10^{21}$ m^{-3}, $\gamma_y = 0$; (**b**) The attenuation curves $H = 1$ µm, $N_D^L = 10 \times 10^{21}$ m^{-3}, $\gamma_x = 0$; (**c**) The attenuation curves $H = 5$ µm, $N_D^L = 10 \times 10^{21}$ m^{-3}, $\gamma_y = 0$; (**d**) The attenuation curves $H = 5$ µm, $N_D^L = 10 \times 10^{21}$ m^{-3}, $\gamma_x = 0$; (**e**) The attenuation curves $H = 10$ µm, $N_D^L = 10 \times 10^{21}$ m^{-3}, $\gamma_y = 0$; (**f**) The attenuation curves $H = 10$ µm, $N_D^L = 10 \times 10^{21}$ m^{-3}, $\gamma_x = 0$.

6. Concluding Remarks

The influence of the Schottky junction on the dispersion and attenuation characteristics of shear horizontal waves in an n-type PSC substrate with a metal layer is the primary

concerns of the present work. According to the surface and interface piezoelectric theories, a new interface effect theoretical model of the Schottky junction is derived based on the physical properties of the Schottky junction. An interface characteristic length that related to the interface piezoelectric parameter is utilized to express the electrically imperfect interface boundary conditions of the Schottky junction. To legitimately confirm the interface characteristic length, the Schottky junction is treated as an electrical gradient layer. Two equivalent mathematical models are established through the optimized spectral method. From the dispersion and attenuation curves of shear horizontal waves and the interface characteristic length calculated and confirmed through these two equivalent mathematical models, the following conclusions can be drawn:

1. Compared with our previous numerical results, the more accurate, wider dimensionless angular frequency intervals and higher orders of the dispersion and attenuation curves of shear horizontal waves can be calculated through these two equivalent mathematical models, which embodies the value of this paper's research work.
2. The second mathematical model is more accurate, but the computational stability and engineering practicality of the first mathematical model is better than that of the second mathematical model.
3. Only the biasing electric field parallel to the Schottky junction can provide evident influence on the attenuation characteristic of shear horizontal waves and enhance the influence of the Schottky junction; adjusting the biasing electric field can regulate attenuation characteristics of shear horizontal waves and optimize the acoustic characteristics of energy harvesters formed by PSC semi-infinite medium

Since the influence of the Schottky junction mainly concentrates on the attenuation characteristic of the shear horizontal wave, the discussion in this paper provides theoretical guidance for the design and manufacture of SAW resonators, energy harvesters, and acoustic wave amplifications [29,30]. Through the first mathematical model and the interface characteristic length, we might consider the propagation characteristics of shear horizontal waves in more complex PSC materials in subsequent work, such as the PSC layered composite structures containing multi-layer Schottky junctions.

Author Contributions: Conceptualization, X.G.; methodology, X.G.; software, X.G.; validation, X.G.; formal analysis, Y.W.; investigation, Y.W.; resources, C.X.; data curation, C.X.; writing—original draft preparation, Z.W.; writing—review and editing, Z.W.; visualization, C.D.; supervision, C.D.; All authors have read and agreed to the published version of the manuscript.

Funding: The whole research is supported by the National Natural Science Foundation of China (12202039) and the Interdisciplinary Research Project for Young Teachers of USTB (Fundamental Research Funds for the Central Universities) (FRF-IDRY-21-006).

Data Availability Statement: The data that support the findings of this study are available on request from the corresponding author, Xiao Guo (xiaoguo@ustb.edu.cn), upon reasonable request.

Conflicts of Interest: The authors declare that they have no conflicts of interest in this work. The authors declare that they do not have any commercial or associative interest that represents a conflict of interest in connection with the work submitted.

Appendix A

To obtain the geometrical thickness and steady electron carrier concentration of the Schottky junction, consider the constitutive equations of the Schottky junction

$$\sigma_{yz}^{L}(y) = c_{yzyz}^{L} u_{z,y}^{L}(y) + e_{yyz}^{L} \phi_{,y}^{L}(y) \tag{A1}$$

$$D_{y}^{L}(y) = e_{yyz}^{L} u_{z,y}^{L}(y) - \varepsilon_{yy}^{L} \phi_{,y}^{L}(y) \tag{A2}$$

$$J_y^L(y) = -q\overline{n}^L(y)\mu_{yy}^L\frac{d\phi^L(y)}{dy} + q\overline{n}^L(y)\mu_{yy}^L\overline{E}_y + qd_{yy}^L\frac{d\overline{n}^L(y)}{dy}, -y_n \le y \le 0 \quad \text{(A3)}$$

Consider the Cauchy stress tensor in the Schottky junction is zero

$$\sigma_{yz}^L(y) = 0, -y_n \le y \le 0 \quad \text{(A4)}$$

Inserting Equation (A1) into Equation (A4) leads to

$$u_{z,y}^L(y) = -\frac{e_{yyz}^L}{c_{yzyz}^L}\phi_{,y}^L(y), -y_n \le y \le 0 \quad \text{(A5)}$$

Inserting Equation (A5) into Equation (A2) leads to

$$D_y^L(y) = -\left(\frac{e_{yyz}^{L2}}{c_{yzyz}^L} + \varepsilon_{yy}^L\right)\phi_{,y}^L(y), -y_n \le y \le 0 \quad \text{(A6)}$$

Consider the governing equations of the Schottky junction

$$D_{y,y}^L = qN_D^L, -y_n \le y \le 0 \quad \text{(A7)}$$

where N_D^L are the donor concentration i.e., the doping concentration, in the lower n-type PSC substrate. Inserting Equation (A7) into Equation (A8) leads to

$$\phi_{,yy}^L(y) = -\frac{qN_D^L}{e_{yyz}^{L2}/c_{yzyz}^L + \varepsilon_{yy}^L}, -y_n \le y \le 0 \quad \text{(A8)}$$

The mathematical solution of ϕ^L can be obtained from Equation (A8)

$$\phi^L(y) = \frac{qN_D^L}{e_{yyz}^{L2}/c_{yzyz}^L + \varepsilon_{yy}^L}\left(-\frac{1}{2}y^2 + Ay + B\right), -y_n \le y \le 0 \quad \text{(A9)}$$

where A and B are two unknown constants. To determine the expression of A, the potential boundary conditions at the lower boundary of the Schottky junction are introduced

$$-\phi_{,y}^L(-y_n) = \overline{E}_y \quad \text{(A10)}$$

Combining Equations (A9) and (A10) leads to

$$\phi^L(y) = \frac{qN_D^L}{e_{yyz}^{L2}/c_{yzyz}^L + \varepsilon_{yy}^L}\left(-\frac{1}{2}y^2 - y_n y + B\right) - \overline{E}_y y, -y_n \le y \le 0 \quad \text{(A11)}$$

The contact potential condition between the upper metal layer and lower n-type PSC substrate is introduced

$$\phi^L(-y_n) - \phi^L(0) = \frac{W^U - W^L}{q} + \overline{E}_y y_n \quad \text{(A12)}$$

Inserting Equation (A1) into Equation (A12) leads to the geometrical thickness of the Schottky junction

$$y_n = \sqrt{\frac{2\left(e_{yyz}^{L2}/c_{yzyz}^L + \varepsilon_{yy}^L\right)(W^U - W^L)}{q^2N_D^L}} \quad \text{(A13)}$$

Consider the electron carrier current density tensor in the Schottky junction is zero

$$J_y^L(y) = 0, -y_n \le y \le 0 \quad \text{(A14)}$$

Inserting Equations (A3) and (A11) into Equation (A14) leads to

$$\overline{n}^L(y) = Cexp\left\{\frac{\mu_{yy}^L}{d_{yy}^L}\left[\frac{qN_D^L}{e_{yyz}^{L2}/c_{yzyz}^L + \varepsilon_{yy}^L}\left(-\frac{1}{2}y^2 - y_n y\right) - 2\overline{E}_y y\right]\right\}, -y_n \le y \le 0 \quad \text{(A15)}$$

The boundary conditions of steady-state carrier concentration are introduced

$$\overline{n}^L(-y_n) = N_D^L \quad \text{(A16)}$$

Combining Equations (A15) and (A16), and $\mu_{yy}^L/d_{yy}^L = q/(k_B T)$ leads to the steady electron carrier concentration of the Schottky junction

$$\overline{n}^L = \begin{cases} N_D^L exp\left\{\frac{q}{k_B T}\left[\frac{qN_D^L}{e_{yyz}^{L2}/c_{yzyz}^L + \varepsilon_{yy}^L}\right.\right. & -y_n \le y \le 0 \\ \left.\left.\left(-\frac{1}{2}y^2 - y_n y - \frac{1}{2}y_n^2\right) - 2\overline{E}_y(y + y_n)\right]\right\} & \\ N_D^L & -\infty < y \le -y_n \end{cases} \quad \text{(A17)}$$

The explicit expressions of coefficient matrices ***A***, ***B***, ***C***, ***D***, and ***F*** in Equation (44) are

$$\boldsymbol{A} = \begin{bmatrix} \boldsymbol{A}_{11}^{lm} & \boldsymbol{O} & \boldsymbol{O} & \boldsymbol{O} \\ \boldsymbol{O} & \boldsymbol{A}_{22}^{lm} & \boldsymbol{O} & \boldsymbol{O} \\ \boldsymbol{O} & \boldsymbol{O} & \boldsymbol{O} & \boldsymbol{O} \\ \boldsymbol{O} & \boldsymbol{O} & \boldsymbol{O} & \boldsymbol{O} \end{bmatrix}, \boldsymbol{B} = \begin{bmatrix} \boldsymbol{O} & \boldsymbol{O} & \boldsymbol{O} & \boldsymbol{O} \\ \boldsymbol{O} & \boldsymbol{O} & \boldsymbol{O} & \boldsymbol{O} \\ \boldsymbol{O} & \boldsymbol{O} & \boldsymbol{O} & \boldsymbol{O} \\ \boldsymbol{O} & \boldsymbol{O} & \boldsymbol{O} & \boldsymbol{B}_{44}^{lm} \end{bmatrix},$$

$$\boldsymbol{C} = \begin{bmatrix} \boldsymbol{C}_{11}^{lm} & \boldsymbol{C}_{12}^{lm} & \boldsymbol{O} & \boldsymbol{O} \\ \boldsymbol{C}_{21}^{lm} & \boldsymbol{C}_{22}^{lm} & \boldsymbol{C}_{23}^{lm} & \boldsymbol{O} \\ \boldsymbol{O} & \boldsymbol{C}_{32}^{lm} & \boldsymbol{C}_{33}^{lm} & \boldsymbol{C}_{34}^{lm} \\ \boldsymbol{O} & \boldsymbol{O} & \boldsymbol{C}_{43}^{lm} & \boldsymbol{C}_{44}^{lm} \end{bmatrix}, \boldsymbol{D} = \begin{bmatrix} \boldsymbol{D}_{11}^{lm} & \boldsymbol{O} & \boldsymbol{O} & \boldsymbol{O} \\ \boldsymbol{O} & \boldsymbol{D}_{22}^{lm} & \boldsymbol{D}_{23}^{lm} & \boldsymbol{O} \\ \boldsymbol{O} & \boldsymbol{D}_{32}^{lm} & \boldsymbol{D}_{33}^{lm} & \boldsymbol{O} \\ \boldsymbol{O} & \boldsymbol{O} & \boldsymbol{D}_{43}^{lm} & \boldsymbol{D}_{44}^{lm} \end{bmatrix},$$

$$\boldsymbol{F} = \begin{bmatrix} \boldsymbol{O} & \boldsymbol{O} & \boldsymbol{O} & \boldsymbol{O} \\ \boldsymbol{O} & \boldsymbol{O} & \boldsymbol{O} & \boldsymbol{O} \\ \boldsymbol{O} & \boldsymbol{O} & \boldsymbol{O} & \boldsymbol{O} \\ \boldsymbol{O} & \boldsymbol{O} & \boldsymbol{O} & \boldsymbol{F}_{44}^{lm} \end{bmatrix} \quad \text{(A18)}$$

where

$$\boldsymbol{A}_{11}^{lm} = \rho^U \int_0^H R_m^U(y) R_l^U(y) dy, \boldsymbol{A}_{22}^{lm} = \rho^L \int_{-\infty}^0 R_m^L(y) R_l^L(y) dy,$$

$$\boldsymbol{B}_{44}^{lm} = \int_{-\infty}^0 R_m^L(y) R_l^L(y) dy,$$

$$\boldsymbol{C}_{11}^{lm} = -c_{yzyz}^U \left(R_m^{U'}(0) R_l^U(0) + R_m^U(H) R_l^{U'}(H) - \int_0^H R_m^U(y) R_l^{U''}(y) dy \right),$$

$$\boldsymbol{C}_{12}^{lm} = c_{yzyz}^U R_m^L(0) R_l^{U'}(0), \boldsymbol{C}_{21}^{lm} = c_{yzyz}^U R_m^{U'}(0) R_l^L(0),$$

$$\boldsymbol{C}_{22}^{lm} = -c_{yzyz}^L \left(R_m^L(0) R_l^{L'}(0) - \int_{-\infty}^0 R_m^L(y) R_l^{L''}(y) dy \right),$$

$$\boldsymbol{C}_{23}^{lm} = e_{yyz}^L \int_{-\infty}^0 R_m^L(y) R_l^{L''}(y) dy,$$

$$\boldsymbol{C}_{32}^{lm} = e_{yyz}^L \left(\int_{-\infty}^0 R_m^L(y) R_l^{L''}(y) dy - R_m^L(0) R_l^{L'}(0) \right),$$

$$\boldsymbol{C}_{33}^{lm} = -\varepsilon_{yy}^L \int_{-\infty}^0 R_m^L(y) R_l^{L''}(y) dy, \boldsymbol{C}_{34}^{lm} = q \int_{-\infty}^0 R_m^L(y) R_l^L(y) dy,$$

$$\boldsymbol{C}_{43}^{lm} = -N_D^L \mu_{yy}^L \left(R_m^{L\prime}(0) R_l^L(0) - R_m^L(0) R_l^{L\prime}(0) + \int_{-\infty}^{0} R_m^L(y) R_l^{L\prime\prime}(y) dy \right),$$

$$\boldsymbol{C}_{44}^{lm} = d_{yy}^L \left(R_m^{L'}(0) R_l^L(0) - R_m^L(0) R_l^{L'}(0) + \int_{-\infty}^{0} R_m^L(y) R_l^{L''}(y) dy \right)$$

$$+ \overline{E}_y \mu_{yy}^L \left(R_m^L(0) R_l^L(0) - \int_{-\infty}^{0} R_m^L(y) R_l^{L\prime}(y) dy \right),$$

$$\boldsymbol{D}_{11}^{lm} = c_{yzyz}^U \int_0^H R_m^U(y) R_l^U(y) dy, \boldsymbol{D}_{22}^{lm} = c_{yzyz}^L \int_{-\infty}^{0} R_m^L(y) R_l^L(y) dy,$$

$$\boldsymbol{D}_{23}^{lm} = e_{yyz}^L \int_{-\infty}^{0} R_m^L(y) R_l^L(y) dy,$$

$$\boldsymbol{D}_{32}^{lm} = e_{yyz}^L \int_{-\infty}^{0} R_m^L(y) R_l^L(y) dy + f_e^L e_{yyz}^L R_m^L(0) R_l^L(0),$$

$$\boldsymbol{D}_{33}^{lm} = -\varepsilon_{yy}^L \int_{-\infty}^{0} R_m^L(y) R_l^L(y) dy, \boldsymbol{D}_{43}^{lm} = -N_D^L \mu_{yy}^L \int_{-\infty}^{0} R_m^L(y) R_l^L(y) dy$$

$$\boldsymbol{D}_{44}^{lm} = d_{yy}^L \int_{-\infty}^{0} R_m^L(y) R_l^L(y) dy, \boldsymbol{F}_{44}^{lm} = \overline{E}_x \mu_{yy}^L \int_{-\infty}^{0} R_m^L(y) R_l^L(y) dy \tag{A19}$$

and

$$R_m^L(0) = 1, R_m^{L'}(0) = \frac{1}{2} + m, \int_{-\infty}^{0} R_m^L(y) R_l^L(y) dy = \delta_{m,l},$$

$$\int_{-\infty}^{0} R_m^{L\prime}(y) R_l^L(y) dy = \frac{1}{2}\delta_{m,l} + h_1(m-l-1),$$

$$\int_{-\infty}^{0} R_m^{L''}(y) R_l^L(y) dy = \frac{1}{4}\delta_{m,l} + (m-l) h_1(m-l-1),$$

$$R_m^U(H) = 1, R_m^U(0) = (-1)^m,\ R_m^{U\prime}(H) = \frac{m(m+1)}{H},$$

$$R_m^{U\prime}(0) = (-1)^{m+1} \frac{m(m+1)}{H}, \int_0^H R_m^U(y) R_l^U(y) dy = \frac{H}{2m+1}\delta_{m,l},$$

$$\int_0^H R_m^{U\prime}(y) R_l^U(y) dy = \begin{cases} \sum_{k=0}^{n} 2\delta_{2k-1,l} & m = 2n \\ \sum_{k=0}^{n} 2\delta_{2k,l} & m = 2n+1 \end{cases},$$

$$\int_0^H R_m^{U''}(y) R_l^U(y) dy$$

$$= \begin{cases} \frac{2m(m+1)}{h} - \frac{2\min(m,l)\cdot[min(m,l)+1]}{h} & m+l \equiv 0\ (mod\ 2) \\ 0 & m+l \equiv 1\ (mod\ 2) \end{cases},$$

$$\delta_{m,l} = \begin{cases} 0 & m \neq l \\ 1 & m = l \end{cases}, h_1(y) = \begin{cases} 0 & y < 0 \\ 1 & y \geq 0 \end{cases} \tag{A20}$$

The explicit expressions of coefficient matrices $\overline{\boldsymbol{A}}$, $\overline{\boldsymbol{B}}$, $\overline{\boldsymbol{C}}$, $\overline{\boldsymbol{D}}$ and $\overline{\boldsymbol{F}}$ in Equation (58) are

$$\overline{\boldsymbol{A}} = \begin{bmatrix} \overline{\boldsymbol{A}}_{11}^{lm} & \boldsymbol{O} & \boldsymbol{O} & \boldsymbol{O} \\ \boldsymbol{O} & \overline{\boldsymbol{A}}_{22}^{lm} & \boldsymbol{O} & \boldsymbol{O} \\ \boldsymbol{O} & \boldsymbol{O} & \boldsymbol{O} & \boldsymbol{O} \\ \boldsymbol{O} & \boldsymbol{O} & \boldsymbol{O} & \boldsymbol{O} \end{bmatrix}, \overline{\boldsymbol{B}} = \begin{bmatrix} \boldsymbol{O} & \boldsymbol{O} & \boldsymbol{O} & \boldsymbol{O} \\ \boldsymbol{O} & \boldsymbol{O} & \boldsymbol{O} & \boldsymbol{O} \\ \boldsymbol{O} & \boldsymbol{O} & \boldsymbol{O} & \boldsymbol{O} \\ \boldsymbol{O} & \boldsymbol{O} & \boldsymbol{O} & \overline{\boldsymbol{B}}_{44}^{lm} \end{bmatrix},$$

$$\overline{\boldsymbol{C}} = \begin{bmatrix} \overline{\boldsymbol{C}}_{11}^{lm} & \overline{\boldsymbol{C}}_{12}^{lm} & \boldsymbol{O} & \boldsymbol{O} \\ \overline{\boldsymbol{C}}_{21}^{lm} & \overline{\boldsymbol{C}}_{22}^{lm} & \overline{\boldsymbol{C}}_{23}^{lm} & \boldsymbol{O} \\ \boldsymbol{O} & \overline{\boldsymbol{C}}_{32}^{lm} & \overline{\boldsymbol{C}}_{33}^{lm} & \overline{\boldsymbol{C}}_{34}^{lm} \\ \boldsymbol{O} & \boldsymbol{O} & \overline{\boldsymbol{C}}_{43}^{lm} & \overline{\boldsymbol{C}}_{44}^{lm} \end{bmatrix}, \overline{\boldsymbol{D}} = \begin{bmatrix} \overline{\boldsymbol{D}}_{11}^{lm} & \boldsymbol{O} & \boldsymbol{O} & \boldsymbol{O} \\ \boldsymbol{O} & \overline{\boldsymbol{D}}_{22}^{lm} & \overline{\boldsymbol{D}}_{23}^{lm} & \boldsymbol{O} \\ \boldsymbol{O} & \overline{\boldsymbol{D}}_{32}^{lm} & \overline{\boldsymbol{D}}_{33}^{lm} & \boldsymbol{O} \\ \boldsymbol{O} & \boldsymbol{O} & \overline{\boldsymbol{D}}_{43}^{lm} & \overline{\boldsymbol{D}}_{44}^{lm} \end{bmatrix},$$

$$\overline{\boldsymbol{F}} = \begin{bmatrix} \boldsymbol{O} & \boldsymbol{O} & \boldsymbol{O} & \boldsymbol{O} \\ \boldsymbol{O} & \boldsymbol{O} & \boldsymbol{O} & \boldsymbol{O} \\ \boldsymbol{O} & \boldsymbol{O} & \boldsymbol{O} & \boldsymbol{O} \\ \boldsymbol{O} & \boldsymbol{O} & \boldsymbol{O} & \overline{\boldsymbol{F}}_{44}^{lm} \end{bmatrix} \tag{A21}$$

where

$$\overline{\boldsymbol{A}}_{11}^{lm} = \rho^U \int_0^H R_m^U(y) R_l^U(y) dy, \overline{\boldsymbol{A}}_{22}^{lm} = \rho^L \int_{-\infty}^0 R_m^L(y) R_l^L(y) dy,$$

$$\overline{\boldsymbol{B}}_{44}^{lm} = \int_{-\infty}^{-y_n} R_m(y) R_l(y) dy,$$

$$\overline{\boldsymbol{C}}_{11}^{lm} = -c_{yzyz}^U \left(R_m^{U'}(0) R_l^U(0) + R_m^U(H) R_l^{U'}(H) - \int_0^H R_m^U(y) R_l^{U''}(y) dy \right),$$

$$\overline{\boldsymbol{C}}_{12}^{lm} = c_{yzyz}^U R_m^L(0) R_l^{U\prime}(0), \overline{\boldsymbol{C}}_{21}^{lm} = c_{yzyz}^U R_m^{U\prime}(0) R_l^L(0),$$

$$\overline{\boldsymbol{C}}_{22}^{lm} = -c_{yzyz}^L \left(R_m^L(0) R_l^{L\prime}(0) - \int_{-\infty}^0 R_m^L(y) R_l^{L''}(y) dy \right),$$

$$\overline{\boldsymbol{C}}_{23}^{lm} = e_{yyz}^L \int_{-\infty}^0 R_m^L(y) R_l^{L''}(y) dy,$$

$$\overline{\boldsymbol{C}}_{32}^{lm} = e_{yyz}^L \left(R_m^{L\prime}(0) R_l^L(0) - R_m^L(0) R_l^{L\prime}(0) + \int_{-\infty}^0 R_m^L(y) R_l^{L''}(y) dy \right),$$

$$\overline{\boldsymbol{C}}_{33}^{lm} = -\varepsilon_{yy}^L \left(R_m^{L'}(0) R_l^L(0) + \int_{-\infty}^0 R_m^L(y) R_l^{L''}(y) dy \right),$$

$$\overline{\boldsymbol{C}}_{34}^{lm} = q \int_{-\infty}^0 R_m^L(y) R_l^L(y) dy,$$

$$\overline{\boldsymbol{C}}_{43}^{lm} = -\mu_{yy}^L N_D^L \int_{-\infty}^{-y_n} R_m^{L''}(y) R_l^L(y) dy, \overline{\boldsymbol{C}}_{44}^{lm} = d_{yy}^L \left(R_m^{L'}(0) R_l^L(0) + \int_{-\infty}^0 R_m^L(y) R_l^{L''}(y) dy \right)$$
$$-d_{yy}^L \int_{-y_n}^0 R_m^{L''}(y) R_l^L(y) dy + \mu_{yy}^L \overline{E}_y \int_{-\infty}^{-y_n} R_m^{L'}(y) R_l(y) dy,$$

$$\overline{\boldsymbol{D}}_{11}^{lm} = c_{yzyz}^U \int_0^H R_m^U(y) R_l^U(y) dy, \overline{\boldsymbol{D}}_{22}^{lm} = c_{yzyz}^L \int_{-\infty}^0 R_m^L(y) R_l^L(y) dy,$$

$$\overline{\boldsymbol{D}}_{23}^{lm} = e_{yyz}^L \int_{-\infty}^0 R_m^L(y) R_l^L(y) dy, \overline{\boldsymbol{D}}_{32}^{lm} = e_{yyz}^L \int_{-\infty}^0 R_m^L(y) R_l^L(y) dy,$$

$$\overline{\boldsymbol{D}}_{33}^{lm} = -\varepsilon_{yy}^L \int_{-\infty}^0 R_m^L(y) R_l^L(y) dy, \overline{\boldsymbol{D}}_{43}^{lm} = -\mu_{yy}^L N_D^L \int_{-\infty}^{-y_n} R_m^L(y) R_l^L(y) dy,$$

$$\overline{\boldsymbol{D}}_{44}^{lm} = d_{yy}^L \int_{-\infty}^{-y_n} R_m^L(y) R_l^L(y) dy, \overline{\boldsymbol{F}}_{44}^{lm} = \mu_{yy}^L \overline{E}_x \int_{-\infty}^{-y_n} R_m^L(y) R_l^L(y) dy \tag{A22}$$

Since the second mathematical model is also a validation of our previous mathematical model, Table A1 summarizes the current work with previous work.

Table A1. The summarization of the current work with previous work.

		The Current Work		Reference [16]
		The First Mathematical Model	**The Second Mathematical Model**	
The constitutive equations	The lower n-type PSC substrate	With the consideration of biasing electric fields		Without the consideration of biasing electric fields
	The upper metal layer	Identical		
The governing equations	The lower n-type PSC substrate	Identical		
	The upper metal layer	Identical		
The surface condition of the upper metal layer		Identical		
Theoretical treatment of the Schottky junction		An electrically imperfect interface	An electrical gradient layer	
Theoretical modeling method		The spectral method	The optimized spectral method	The state transfer equation method
The numerical calculation of dispersion and attenuation curves		Generalized eigenvalue problems		Searching for complex roots of complex transcendental equations

References

1. Cao, X.; Hu, S.; Liu, J.; Shi, J. Generalized Rayleigh surface waves in a piezoelectric semiconductor substrate. *Meccanica* **2019**, *54*, 271–281. [CrossRef]
2. Liu, Y.; Lin, S.; Li, Y.; Li, C.; Liang, Y. Numerical investigation of shear horizontal wave in layered composite piezoelectric structures using the SIGA-PML approach. *Compos. Part B* **2019**, *158*, 230–238. [CrossRef]
3. Singh, A.K.; Kumari, R.; Ray, A.; Chattopadhyay, A. Love-type waves in a piezoelectric-viscoelastic bimaterial composite structure due to an impulsive point source. *Int. J. Mech. Sci.* **2019**, *152*, 613–629. [CrossRef]
4. Goyal, R.; Kumar, S. Quantifying viscoelastic, piezoelectric and couple stress effects on Love-type wave propagation. *Smart Mater. Struct.* **2019**, *28*, 105021. [CrossRef]
5. Yang, G.; Zhang, M.; Hu, J.; Huang, B.; Xu, M.; Zhu, Z.; Du, J. Effects of initial stress on band gap of Love waves in a layered domain inverted phononic crystal structure. *Ultrasonics* **2020**, *106*, 106145. [CrossRef] [PubMed]
6. Luo, Y.; Zhang, C.; Chen, W.; Yang, J. Piezotronic Effect of a Thin Film With Elastic and Piezoelectric Semiconductor Layers Under a Static Flexural Loading. *J. Appl. Mech.* **2019**, *86*, 051003. [CrossRef]
7. Liang, Y.; Hu, Y. Influence of Doping Concentration on the Outputs of a Bent ZnO Nanowire. *IEEE Trans. Ultrason. Ferroelectr. Freq. Control* **2019**, *66*, 1793–1797. [CrossRef]
8. Qu, Y.; Jin, F.; Yang, J. Torsion of a piezoelectric semiconductor rod of cubic crystals with consideration of warping and in-plane shear of its rectangular cross section. *Mech. Mater.* **2022**, *172*, 104407. [CrossRef]
9. He, J.; Ye, W. Fully-coupled piezoelectric field in the semiconductor heterostructure with an ellipsoidal anisotropic inhomogeneity. *Mech. Mater.* **2023**, *187*, 104837. [CrossRef]
10. Tian, R.; Nie, G.; Liu, J.; Pan, E.; Wang, Y. On Rayleigh waves in a piezoelectric semiconductor thin film over an elastic half-space. *Int. J. Mech. Sci.* **2021**, *204*, 106565. [CrossRef]
11. Jiao, F.; Wei, P.; Zhou, X.; Zhou, X. The dispersion and attenuation of the multi-physical fields coupled waves in a piezoelectric semiconductor. *Ultrasonics* **2019**, *92*, 68–78. [CrossRef]
12. Jiao, F.; Wei, P.; Zhou, Y.; Zhou, X. Wave propagation through a piezoelectric semiconductor slab sandwiched by two piezoelectric half-spaces. *Eur. J. Mech./A Solids* **2019**, *75*, 70–81. [CrossRef]
13. Tian, R.; Liu, J.; Pan, E.; Wang, Y. SH waves in multilayered piezoelectric semiconductor plates with imperfect interfaces. *Eur. J. Mech./A Solids* **2020**, *81*, 103961. [CrossRef]
14. Al-Ahmadi, N.A. Schottky barrier inhomogeneities at the interface of different epitaxial layer thicknesses of n-GaAs/Ti/Au/Si: Al0.33Ga0.67As. *Heliyon* **2020**, *6*, e04852. [CrossRef]
15. Yang, M.M.; Luo, Z.D.; Mi, Z.; Zhao, J.; Sharel P., E.; Alexe, M. Piezoelectric and pyroelectric effects induced by interface polar symmetry. *Nature* **2020**, *377*, 584. [CrossRef]
16. Xu, C.; Wei, P.; Wei, Z.; Guo, X. Shear horizontal wave in a piezoelectric semiconductor substrate covered with a metal layer with consideration of Schottky junction effects. *Appl. Math. Model.* **2022**, *109*, 509–518. [CrossRef]

17. Pang, Y.; Feng, W.; Liu, J.; Zhang, C. SH wave propagation in a piezoelectric/piezomagnetic plate with an imperfect magnetoelectroelastic interface. *Waves Random Complex Media* **2019**, *29*, 580–594. [CrossRef]
18. Song, H.X.; Ke, L.L.; Su, J.; Yang, J.; Kitipornchai, S.; Wang, Y.S. Surface effect on the contact problem of a piezoelectric half-plane. *Int. J. Solids Struct.* **2020**, *185–186*, 380–393. [CrossRef]
19. Wang, X.; Li, P.; Jin, F. A generalized dynamic model of nanoscale surface acoustic wave sensors and its applications in Love wave propagation and shear-horizontal vibration. *Appl. Math. Model.* **2019**, *75*, 101–115. [CrossRef]
20. Zhu, F.; Pan, E.; Qian, Z.; Wang, Y. Dispersion curves, mode shapes, stresses and energies of SH and Lamb waves in layered elastic nanoplates with surface/interface effect. *Int. J. Eng. Sci.* **2019**, *142*, 170–184. [CrossRef]
21. Enzevaee, C.; Shodja, H.M. Torsional surface wave propagation in a transversely isotropic FG substrate with piezoelectric over-layer within surface/interface theory. *Acta Mech.* **2020**, *231*, 2203–2216. [CrossRef]
22. Guo, X.; Wei, P.; Xu, M.; Lan, M. Dispersion relations of anti-plane elastic waves in micro-scale one dimensional piezoelectric semiconductor phononic crystals with the consideration of interface effect. *Mech. Mater.* **2021**, *161*, 104000. [CrossRef]
23. Zhang, Q.; Li, M.; Zhao, M. Dynamic analysis of a piezoelectric semiconductor nanoplate with surface effect. *Mater. Today Commun.* **2022**, *33*, 104406. [CrossRef]
24. Li, D.; Li, S.; Zhang, C.; Chen, W. Propagation characteristics of the shear horizontal wave in piezoelectric semiconductor nanoplates incorporating surface effect. *Int. J. Mech. Sci.* **2023**, *247*, 108201. [CrossRef]
25. Karpfinger, F.; Gurevich, B.; Bakulin, A. Modeling of wave dispersion along cylindrical structures using the spectral method. *J. Acoust. Soc. Am.* **2008**, *124*, 859. [CrossRef] [PubMed]
26. Li, K.; Jing, S.; Yu, J.; Zhang, X.; Zhang, B. The Complex Rayleigh Waves in a Functionally Graded Piezoelectric Half-Space: An Improvement of the Laguerre Polynomial Approach. *Materials* **2020**, *13*, 2320. [CrossRef]
27. Li, K.; Jing, S.; Yu, J.; Zhang, B. Complex Rayleigh Waves in Nonhomogeneous Magneto-Electro-Elastic Half-Spaces. *Materials* **2021**, *14*, 1011. [CrossRef]
28. Pang, Y.; Xu, C.; Ge, T.; Feng, W. Shear horizontal wave propagation along a periodic metal grating surface of a magneto-electro-elastic substrate. *J. Appl. Phys.* **2019**, *125*, 165104. [CrossRef]
29. Patel, R.; Adhikari, M.S.; Boolchandani, D. Active area optimization of film bulk acoustic resonator for improving performance parameters. *Electron. Lett.* **2020**, *56*, 1191–1194. [CrossRef]
30. Hu, Y.; Dong, B.; Lei, L.; Wang, Z.; Ruan, S. High-order harmonic film bulk acoustic resonator based on a polymer reflector. *Sensors* **2022**, *22*, 7439. [CrossRef]

Disclaimer/Publisher's Note: The statements, opinions and data contained in all publications are solely those of the individual author(s) and contributor(s) and not of MDPI and/or the editor(s). MDPI and/or the editor(s) disclaim responsibility for any injury to people or property resulting from any ideas, methods, instructions or products referred to in the content.